Advances in Water Resources 171 (2023) 104355

Contents lists available at ScienceDirect

Advances in Water Resources

journal homepage: www.elsevier.com/locate/advwatres

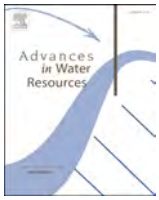

Curvature-induced secondary flow in 2D depth-averaged hydro-morphodynamic models: An assessment of different approaches and key factors

Tommaso Lazzarin *, Daniele P. Viero

Department of Civil, Environmental and Architectural Engineering, University of Padova, via Marzolo 9, 35131 Padova, Italy

ARTICLE INFO

Keywords:
Secondary currents
Helical flow
Sharp bend saturation
Shallow water equations
Hydro-morphodynamic model
Free-surface flow

ABSTRACT

Curvature-induced secondary flows are ubiquitous in nature and have long attracted scientist attention. Modelling such kind of secondary flows is not straightforward. While full 3D models fit the purpose at the cost of great computational demand, simplified models often pose concerns about their effectiveness and the representation of key processes. In the present study, helical flow secondary currents are included in a two-dimensional depth-averaged hydro-morphodynamic model on cartesian unstructured meshes. The non-uniform vertical distribution of velocity in streamwise and spanwise directions is accounted for introducing dispersive terms in the shallow water equations, an anisotropic diffusivity tensor in the advection-diffusion equation, and a correction to the direction of bed shear stress and bedload transport. Different approaches available in the literature are recast in similar form and compared to each other in terms of flow field, tracer transport, and bed evolution, using data from laboratory experiments and real-world case studies. The model includes a novel, pure 2D implementation of the non-linear saturation mechanism that limits the growth of secondary flows in relatively sharp bends. A substantial part of the paper is devoted to discuss key factors in secondary flow modelling, including implementation tricks, guidelines to mesh design, the suitability of local and non-local approaches, and the role of bathymetry. The final goal is to provide useful guidelines for 2D hydro- and morphodynamic modelling in river bends.

1. Introduction

In river and channel bends, the interplay between the curvature of streamlines in the horizontal plane and the non-uniformity of streamwise velocity along the vertical produces a streamwise-oriented helical flow, because of an imbalance between the outward centrifugal acceleration and the inward pressure gradient (Blanckaert and de Vriend, 2010; Falcon, 1984; van Balen et al., 2010). This curvature-induced secondary current, which acts to deviate the high-velocity thread from the inner to the outer bank (Ahmadi et al., 2009; Bolla Pittaluga et al., 2009; Johannesson and Parker, 1989a; Lien et al., 1999; Seminara, 2006; Shimizu et al., 1990; Wu et al., 2004, 2005), has long attracted scientist attention (e.g., Boussinesq, 1868; Thomson, 1877; the tea leaves of Einstein, 1926; see also Bowker, 1988) because of interesting fundamental implications in shaping the riverbed bathymetry, in contributing to bank erosion and meander migration, in enhancing mixing and dispersions of heat and solutes, in increasing flow resistance, etc. (Constantinescu et al., 2013; Demuren and Rodi, 1986; Duan, 2004; Gu et al., 2016; Iwasaki et al., 2016; Jang and Shimizu, 2005; Koken et al., 2013; Lai et al., 2012; Papanicolaou et al., 2007; Termini, 2014).

Modelling the secondary currents in river bends is an important and challenging issue. The most natural way of modelling secondary currents is employing full three-dimensional (3D) models, which naturally resolve curvature-induced helical flows (Keylock et al., 2012). Starting from pioneering applications in the '70s (Leschziner and Rodi, 1979; Pratap and Spalding, 1975), the increased computational power has now allowed modelling long stretches of natural rivers with full 3D Computational Fluid Dynamics (CFD) tools, but the need of suitable computing facilities and of large computational time still hinder their widespread application (Fischer-Antze et al., 2008; Horna-Munoz and Constantinescu, 2018).

The search for efficient strategies to account for curvature-induced secondary flow in reduced-order hydraulic models, started by Van Bendegom (1947) by looking at the flow field in a single bend, has so far

* Corresponding author.
E-mail address: tommaso.lazzarin@phd.unipd.it (T. Lazzarin).

https://doi.org/10.1016/j.advwatres.2022.104355
Received 6 July 2022; Received in revised form 19 November 2022; Accepted 21 November 2022
Available online 23 November 2022

produced many different approaches and modelling strategies (Blanckaert and de Vriend, 2010; Camporeale et al., 2007; Lane, 1998). Most of these are linear (or weakly non-linear) models, valid for low curvatures of the river axis and slowly varying bed topography, hence suitable to model long-term migration of large-scale meandering rivers.

To meet the specific needs of practical engineering problems involving fluvial hydro- and morpho-dynamics, two-dimensional (2D) free-surface shallow water models still represent a valid compromise between efficiency and effectiveness (Shaheed et al., 2021; Uijttewaal, 2014). In 2D depth-averaged models, the vertical velocity profile is assumed implicitly, and it is commonly taken to be constant (Bates, 2022; Ghamry and Steffler, 2002). To account for the effects of secondary flows in channel bends, the shallow water equations (SWEs) are enriched with dispersive stresses (Bora and Khalita, 2020; Camporeale et al., 2021; Song et al., 2012), which parameterize the momentum transfer produced by the streamwise-oriented helical flow.

The simplest approach to account for curvature-induced secondary flows in 2D models assumes instantaneous adaptation of secondary flow intensity to the driving curvature. The dispersive stresses are linked to the local streamline curvature directly (Begnudelli et al., 2010; Duan, 2004; Guan et al., 2016; Lien et al., 1999; Song et al., 2012). Actually, the problem is further complicated because the streamline curvature generates secondary flow progressively, i.e., with a phase-lag due to inertia, and the helical flow is subject to different dissipative mechanisms as well (Blanckaert and de Vriend, 2003, 2004). The lagged formation of helical flow in steady state applications was simulated by introducing an adaptation length (Blanckaert and de Vriend, 2003; De Vriend, 1981; Johannesson and Parker, 1989b; Kikkawa et al., 1976; Rozovskii, 1957; Wu et al., 2004, 2005). A more rigorous and general approach requires solving a transport-diffusion equation for vorticity (or angular momentum), with centrifugal force and resistance mechanisms acting as source and sink terms, respectively (Bernard and Schneider, 1992; Einstein and Li, 1958; Ikeda and Nishimura, 1986; Kalkwijk and Booij, 1986; Odgaard, 1986). At the cost of additional computational demand, this approach doesn't suffer from local singularities in the curvature field and reproduces the slow decay of the helical flow, which vanishes at a long distance downstream of a bend (Bai et al., 2019).

Concerning the implementation of the above methods, modelling approaches proliferated with regard to: *i)* the basic conservation principle, such as extra equations from the Navier Stokes equations (Ghamry and Steffler, 2002; Jin and Steffler, 1993; Yeh and Kennedy, 1993), reduced versions of the momentum equation in the transversal direction (e.g., Kalkwijk and Booij, 1986; Odgaard, 1986), or the conservation of angular momentum in the transversal plane (e.g., Bernard and Schneider, 1992; Finnie et al., 1999); *ii)* the vertical profile for the streamwise velocity component, either logarithmic (Bernard and Schneider, 1992; De Vriend, 1977, 1981; Kitanidis and Kennedy, 1984; Shimizu et al., 1990) or power-law (Odgaard, 1986; Wu et al., 2004; Yeh and Kennedy, 1993); *iii)* the vertical profile for the spanwise velocity component, typically linear with zero mean (Odgaard, 1986), albeit with variations (De Vriend, 1977, 1981; Kikkawa et al., 1976; Shin and Seo, 2021); *iv)* the way in which local curvature is estimated and possibly filtered to avoid numerical instabilities (Abad et al., 2008; Begnudelli et al., 2010); *v)* the use of boundary-fitted orthogonal curvilinear grids, which naturally allow evaluating longitudinal and transversal terms (e.g., Blanckaert and de Vriend, 2003; Demuren, 1993), as opposed to general-purpose unstructured meshes in a Cartesian reference frame that are more flexible in case of unevenly curved bends and wandering riverbeds (Jin and Steffler, 1993; Nikora and Roy, 2011); *vi*) the treatment of impervious banks using either the free- or no-slip condition, each one entailing specific pros and cons (Blanckaert, 2001).

In general, the basic model assumptions limit the scope of such 2D models to the case of mild curvatures. Indeed, in the case of sharp bends, curvature-induced secondary flows are characterized by relevant non-linear feedbacks. The helical flow, with its outward transport of streamwise momentum, modifies both the horizontal pattern and the vertical profiles of flow velocity: the high-velocity thread is moved outward, and the vertical profile is flattened, which means weakening the helical flow production mechanism (Blanckaert, 2009; Blanckaert and de Vriend, 2003; Blanckaert and Graf, 2004; Wei et al., 2016). This feedback-based non-linear process, referred to as saturation of secondary flow, has been assessed quite recently, and its implementation in 2D depth-averaged models is still in its infancy (Guan et al., 2016; Ottevanger et al., 2012; Qin et al., 2019; Shin and Seo, 2021; Xiao et al., 2022).

Finally, the implementation of 2D models accounting for curvature-induced secondary flows, as well as their application to laboratory and real-world case studies, lead to face many other subtle factors. Examples are the proper inclusion of high spatial gradients of water depth associated to compound cross-sections and irregular bathymetries, the computation of dispersive stresses at the wet/dry interface or at the mesh (lateral) boundaries, the need of accounting for lateral wall friction (particularly for laboratory applications with rectangular cross-sections), effective strategies to employ coarser computational meshes, etc.

The present study aims at providing a comprehensive assessment of curvature-induced secondary flows in the frame of general-purpose, depth-averaged 2D models for river hydro- and morpho-dynamics on cartesian (i.e., not curvilinear) coordinate systems. Different parameterizations available in the technical literature are recast in similar form and implemented in a 2D finite-element hydrodynamic model, for both the cases of instantaneous adaptation of helical flow intensity and of transport of streamline vorticity. The saturation of secondary flow in the case of strong curvatures is modelled introducing a pure 2D extension of the model by Blanckaert and de Vriend (2003); saturation effects can be accounted for with any of the approaches for secondary flow implemented in the model. The hydrodynamic module for curvature-induced secondary flows is then integrated with a module for transport of passive tracers, and with a morphodynamic module solving for the bedload sediment transport.

The paper is organized as follows. The theoretical models for curvature-induced flows are presented in Sect. 2, along with an in-depth description of implementation techniques. The model is verified against several laboratory experiments, both with fixed and movable bed (Sect. 3). A model application to a real case-study (Po River) is used to assess some key factors in 2D depth-averaged hydro- and morphodynamic modelling of real rivers. The relevant aspects emerged in this study are then discussed in light of the recent advances on the subject and of open issues (Sect. 4). A set of conclusions closes the paper.

2. Accounting for curvature-induced secondary flows in 2D models

2.1. Shallow water equations with dispersive stresses

On a horizontal Cartesian frame with axes (x, y), under the hypothesis of hydrostatic pressure distribution, the depth-averaged Navier-Stokes equations, commonly known as De Saint Venant or shallow water equations (SWEs), read:

$$\begin{aligned}
&\frac{D}{Dt}\left(\frac{q_x}{Y}\right) - \frac{1}{Y}\left(\frac{\partial \mathrm{Re}_{xx}}{\partial x} + \frac{\partial \mathrm{Re}_{xy}}{\partial y}\right) + \frac{1}{Y}\left(\frac{\partial D_{xx}}{\partial x} + \frac{\partial D_{xy}}{\partial y}\right) + \frac{\tau_{bx}}{\rho Y} + g\,\frac{\partial h}{\partial x} = 0 \\
&\frac{D}{Dt}\left(\frac{q_y}{Y}\right) - \frac{1}{Y}\left(\frac{\partial \mathrm{Re}_{xy}}{\partial x} + \frac{\partial \mathrm{Re}_{yy}}{\partial y}\right) + \frac{1}{Y}\left(\frac{\partial D_{yx}}{\partial x} + \frac{\partial D_{yy}}{\partial y}\right) + \frac{\tau_{by}}{\rho Y} + g\,\frac{\partial h}{\partial y} = 0 \\
&\eta(h)\frac{\partial h}{\partial t} + \frac{\partial q_x}{\partial x} + \frac{\partial q_y}{\partial y} = 0
\end{aligned} \tag{1}$$

where t is time, D/Dt is the material (Lagrangian) time derivative, $\mathbf{q} = (q_x, q_y)$ are the depth-integrated velocity components, Y is the equivalent water depth (i.e., water volume per unit area, Defina, 2000), Re are the

Reynolds turbulent stresses in the horizontal plane, (τ_{bx}, τ_{by}) are the bed shear stress components, ρ is the water density, g is gravity, and h is the water surface elevation over a datum. In the continuity equation, $\eta(h) \in]0,1]$ is a depth-dependent storage coefficient defined as the wet area fraction (Defina, 2000). The dispersive stresses D_{xx}, D_{xy}, and D_{yy} emerge from the integration of a non-uniform vertical distribution of velocity over the water depth, and are defined as

$$\begin{aligned} D_{xx} &= \int_0^Y [u'(z)]^2 \, dz \\ D_{xy} = D_{yx} &= \int_0^Y u'(z) v'(z) dz \\ D_{yy} &= \int_0^Y [v'(z)]^2 \, dz \end{aligned} \tag{2}$$

where the apostrophe denotes the difference between the real and the depth-averaged velocity component (note that the velocity vector is here defined as $\mathbf{w} = (u, v) = \mathbf{q}/Y$):

$$\begin{aligned} u'(z) &= u(z) - u \\ v'(z) &= v(z) - v \end{aligned} \tag{3}$$

Dispersive stress terms thus account for the subscale spatial variations of the unresolved velocity field. To obtain close-form expressions of the dispersive terms, it is convenient to use a local (s, n) reference frame, with s the longitudinal (streamwise) and n the transversal (spanwise) directions (see Fig. 1a), and to assume simple vertical distributions of the flow velocity components along s and n. Among the different expressions used in previous studies, a power law distribution can be assumed for the streamwise component, w_s, which allows for a simpler derivation of dispersive stresses. According to Odgaard (1986):

$$\frac{w_s(z)}{w} = \frac{m+1}{m} \left(\frac{z}{Y}\right)^{\frac{1}{m}} \tag{4}$$

being $w = \sqrt{u^2 + v^2}$ the magnitude of the depth-averaged velocity and m a friction parameter ($m = \chi\kappa / g^{1/2}$ with χ the Chezy coefficient and $\kappa = 0.4$ the von Karman constant). For the spanwise velocity component, w_n, a linear profile with zero mean is commonly used (Jin and Steffler, 1993; Kalkwijk and Booij, 1986; Odgaard, 1986):

$$\frac{w_n(z)}{w} = v_{ns}^* \left(\frac{2z}{Y} - 1\right) \tag{5}$$

where $v_{ns}^* = v_{ns}/w$ is the non-dimensional transversal velocity component at the free-surface. Integration on the water depth provides (Begnudelli et al., 2010; Lien et al., 1999; Wu et al., 2004)

$$\begin{aligned} D_{ss} &= Y \frac{w^2}{m(2+m)} \\ D_{sn} = D_{ns} &= Y \frac{w^2}{1+2m} v_{ns}^* \operatorname{sign}(R) \\ D_{nn} &= Y \frac{\left(v_{ns}^* \, w\right)^2}{3} \end{aligned} \tag{6}$$

being R the radius of curvature of depth-averaged streamlines (R is positive for clockwise bends in the flow direction, and negative vice-versa). Finally, these terms are rotated into the (x, y) coordinate frame by expressing the rotation matrix in terms of velocity components, to read

$$\begin{aligned} D_{xx} &= D_{ss} \frac{u^2}{w^2} - 2D_{sn} \frac{uv}{w^2} + D_{nn} \frac{v^2}{w^2} \\ D_{xy} = D_{yx} &= D_{ss} \frac{uv}{w^2} + D_{sn} \left(\frac{u^2 - v^2}{w^2}\right) - D_{nn} \frac{uv}{w^2} \\ D_{yy} &= D_{ss} \frac{v^2}{w^2} + 2D_{sn} \frac{uv}{w^2} + D_{nn} \frac{u^2}{w^2} \end{aligned} \tag{7}$$

Lien et al. (1999) reported an equivalent derivation of these terms for the case of a logarithmic vertical profile of streamwise velocity.

It's worth noting that the net contribution to momentum (Eqs. (1)) of dispersive stresses D_{ij}, with i and j denoting either x or y, depends on their spatial derivatives rather than on their magnitude. Concerning the role of the single dispersive terms, D_{ss} does not depend on the secondary flow; it acts in the streamwise direction by hindering both spatial acceleration and deceleration. The mixed D_{sn} term is the most important term for simulating secondary flows; its spatial gradient may lead to additional resistance at the inner side of bends and to acceleration at the outer side of bends (Dietrich and Smith, 1983), thus accounting for the effect of outward momentum transfer ascribed to the helical flow. D_{nn} may produce a spanwise net stress that, depending on the spanwise gradient of flow velocity (w) and secondary flow intensity (v_{ns}^*), may lead to a larger free-surface transversal slope.

2.2. Instantaneous-adaptation and vorticity-transport approaches

The dispersive stresses for curvature-induced secondary flows, which depend on the helical flow intensity, can be expressed in terms of non-dimensional spanwise velocity component at the free-surface, v_{ns}^*. Basically, v_{ns}^* can be evaluated using two different approaches: *i)* a local approach, which implies instantaneous adaptation of the helical flow intensity to the local flow features, and *ii)* a vorticity-transport approach, which accounts for generation, transport, and dissipation of the helical flow.

In the local approach, which is simpler and less computationally demanding, v_{ns}^* is a direct function of the local water depth, velocity, and

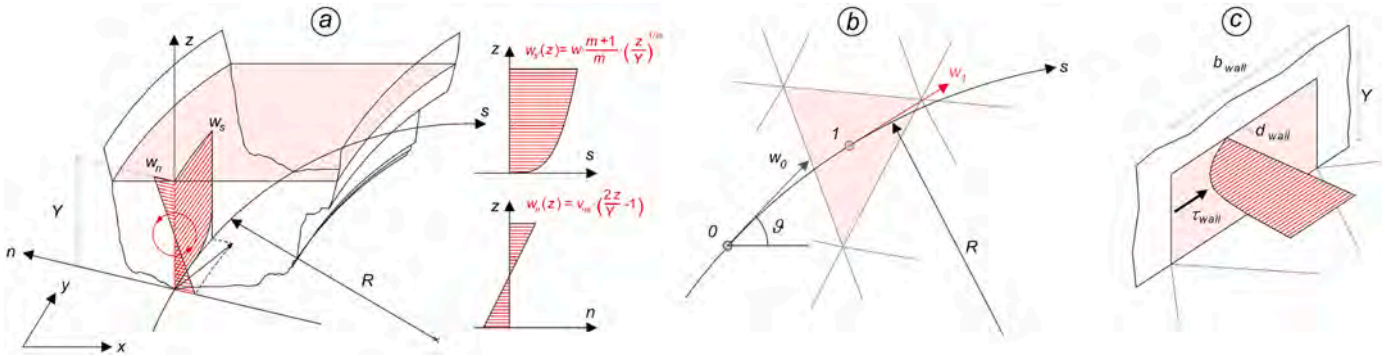

Fig. 1. a) Schematics of main and secondary flows in a channel bend, with notation. b) Estimation of the local streamline curvature. c) Model for wall friction.

streamline curvature. As a major drawback, the local approach does not consider the inertia of secondary flow, and the spatially distributed field of v_{ns}^* becomes particularly sensible to local variations of flow field and streamline curvature, particularly in the vicinity of sharp boundaries (e.g., bridge piers, abutments).

The vorticity-transport approach models the helical flow in terms of streamwise vorticity component, which emerges from the non-uniformity of the spanwise velocity (Einstein and Li, 1958). Usually, rather than solving the complete equation for three-dimensional vorticity vector (Blackaert and de Vriend, 2004), depth-average simplified versions of the vorticity equations are solved for the streamwise component of vorticity, ω (Finnie et al., 1999; Uchida and Fukuoka, 2014). The general form of the transport equation for streamwise vorticity in the (x, y) horizontal plane is:

$$\frac{D\omega}{Dt} = \Omega_{PROD} - \Omega_{DISS} \tag{8}$$

in which Ω_{PROD} is a production term depending on the imbalance between the centrifugal acceleration and the transversal pressure gradient, and Ω_{DISS} is a dissipation term that derives from the bottom stresses (Farhadi et al., 2018; Nezu, 2005). Several formulations have been proposed in the technical literature to estimate the production and dissipation terms of Eq. (8). Although formally different, being obtained from different basis assumptions, they all share a similar structure, as shown in the following.

Noting that the streamwise vorticity component, ω, is twice the angular velocity, Ω, and assuming the linear profile for spanwise velocity of Eq. (5), it results:

$$\omega = 2\Omega = 2\frac{v_{ns}}{Y/2} = 4\frac{v_{ns}}{Y} \tag{9}$$

Under the hypothesis of slowly-varying water depth, Eq. (8) can be written directly in terms of v_{ns} in the general form

$$\frac{Dv_{ns}}{Dt} = f_D k_P \frac{w^2}{R} - k_D \frac{v_{ns} w}{Y} \tag{10}$$

being k_P and k_D production and dissipation coefficients, whose formulation depends on the basic conservation principle; f_D is a coefficient introduced to account for non-linearity in the production of helical flow (see Sect. 2.3).

Kalkwijk and Booij (1986) derived a transport-diffusion equation starting from the momentum equation in the transversal direction and using a logarithmic vertical profile for streamwise velocity. This approach is also implemented in Delft3D, with a slightly different formulation for the production term (see Chavarrías et al., 2019). A similar approach has been proposed by Odgaard (1986), which used a power law (Eq. (4)) for the vertical profile of streamwise velocity. Actually, both these studies worked with the assumption of steady state, yet the generalization to unsteady flow is straightforward.

Bernard and Schneider (1992) obtained the transport-diffusion equation by imposing angular momentum conservation on a cross-section and assuming a logarithmic vertical profile for the longitudinal velocity component; in the present work, for the sake of simplicity, the same approach has been reformulated using the power law in Eq. (4).

Eq. (10) can be used to estimate the transversal surface velocity v_{ns}^* for both the vorticity-transport approach and the instantaneous-adaptation approach. Indeed, the instantaneous-adaptation approach implicitly assumes that an equilibrium condition is locally attained elsewhere, which is equivalent to assume that the material derivative of streamwise vorticity (i.e., the left-hand side term in Eq. (10)) vanishes. In this case, v_{ns}^* can be evaluated directly (and locally) as

$$v_{ns}^* = \frac{v_{ns}}{w} = f_D \frac{k_P}{k_D} \frac{Y}{R} \tag{11}$$

Compared to the local approach, which allows estimating the transversal velocity calculating production dissipation terms solely, the vorticity-transport method has a higher computational cost since the transport Eq. (10) must also be solved.

Table 1 reports the different expressions for production and dissipation terms available in the literature, also expressed according to the form of Eqs. (10) and (11). In Fig. 2a, the magnitude of the transversal velocity component at the free-surface is plotted for different value of the Strickler roughness coefficient, K_s. The Bernard and Schneider (1992) model, reformulated assuming a power law vertical profile (red dashed line) is very similar to their original, lag-law based model (red continuous line). The model by Odgaard (1986) shows an opposite trend with respect to that of Kalkwijk and Booij (1986). By increasing values of K_s (i.e., moving toward smoother beds), the vertical profile of streamwise velocity component is progressively flatter, which entails a reduced production of helical flow; yet, a smoother bed also entails reduced resistances to spiral motion. The two above models give different weight to these two opposing factors.

2.3. Saturation of secondary flows

In Eq. (10), as well as in Eq. (11), assuming $f_D = 1$ leads to linear models in which the intensity of secondary flow increases indefinitely with the streamline curvature (Camporeale et al., 2007; Song et al., 2012). This is not the real case, particularly for higher curvature ratios Y/R, because of the so-called saturation effect (Bai et al., 2019; Blanckaert, 2009; Blanckaert and de Vriend, 2003). The dampening factor $f_D \in [0,1]$ is introduced in Eq. (10) to reduce the production term in all the formulation here implemented when the saturation mechanism plays a role.

Blanckaert and de Vriend (2003) proposed a parameterization in

Table 1
Collection of the main formulations for secondary flow proposed in the literature. Ω, I, and v_{ns} measure the secondary flow intensity. In the Bernard and Schneider (1992) formulation, ω is the streamwise vorticity, C_F is a friction parameter, C_A, C_B, C_C, C_2 are model parameters that are combined in the production, A_S, and decay, D_S, coefficients. In the Kalkwijk and Booji (1986) formulation, $k_b = k_b(s)$ is a calibration parameter that accounts for the phase lag.

	Bernard and Schneider (1992)	Kalkwijk and Booji (1986)	Odgaard (1986)
Derived from	Angular Momentum Conservation on Transversal Section	Steady state momentum equation in the transversal direction	Steady state momentum equation in the transversal direction
Transported quantity	$\Omega = \frac{C_A C_B C_2 \omega}{12}$	$I = k_b \frac{wY}{R}$	$v_{ns} = \frac{2m+1}{2\kappa^2 m}\frac{wY}{R}$
Expression for transversal velocity at the free surface	$v_{ns} = \frac{Y\omega}{4} = \frac{Y}{4}\frac{12\Omega}{C_A C_B C_2}$	$v_{ns} = 3\frac{I}{\kappa^2}\left(\frac{1}{2} - \frac{1}{m}\right)$	as above
Original transport-equation	$\frac{D\Omega}{Dt} = \frac{1}{6}\frac{(wC_AC_2)^2}{RY}\sqrt{C_F} - 3C_C\sqrt{C_F}\frac{\Omega w}{Y}$	$\frac{d(k_b\frac{wY}{R})}{ds} = \frac{2\kappa^2}{m-2}\frac{w}{R}(1-k_b)$	$\frac{dv_{ns}}{ds} = \frac{2m+1}{m(m+1)}\frac{w}{R} - \frac{2\kappa^2}{m+1}\frac{v_{ns}}{Y}$
Normalized transport-equation	$\frac{Dv_{ns}}{Dt} = \frac{\sqrt{6A_S}}{2}\frac{\kappa}{m}\frac{w^2}{R} - D_S\frac{\kappa}{m}\frac{wv_{ns}}{Y}$	$w\frac{dv_{ns}}{ds} = \frac{3}{m}\frac{w^2}{R} - \frac{2\kappa^2}{m-2}\frac{wv_{ns}}{Y}$	$w\frac{dv_{ns}}{ds} = \frac{2m+1}{m(m+1)}\frac{w^2}{R} - \frac{2\kappa^2}{m+1}\frac{wv_{ns}}{Y}$
Transversal velocity at equilibrium	$v_{ns}^* = \frac{\sqrt{6A_S}}{2D_S}\frac{Y}{R}$	$v_{ns}^* = \frac{3}{2}\frac{(m-2)}{m\kappa^2}\frac{Y}{R}$	$v_{ns}^* = \frac{2m+1}{2\kappa^2 m}\frac{Y}{R}$

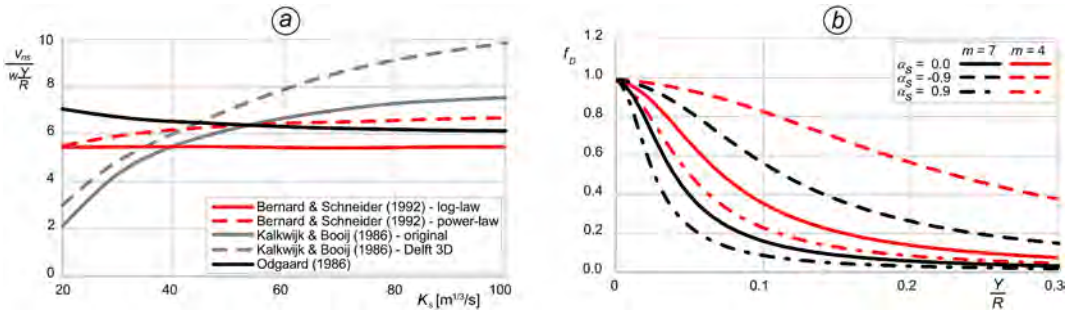

Fig. 2. a) Magnitude of the transversal velocity at the free-surface, v_{ns}, scaled by $w(Y/R)$, evaluated with different approaches using eq. (11) with $f_D = 1$. b) Dampening factor for vorticity production, f_D, for different values of the friction parameter, m, and the normalized spanwise gradient of streamwise velocity, α_s.

which f_D is a function of the bend parameter β, which in turn depends on the normalized transversal gradient of the depth averaged velocity, α_s:

$$f_D = 1 - \exp\left(-\frac{0.4}{1.05\beta^3 - 0.89\beta^2 + 0.5\beta}\right)$$
$$\beta = \sqrt{\frac{Y}{|R|}}\left(\frac{0.41}{m}\right)^{-0.55}(\alpha_s + 1)^{0.25} \quad (12)$$
$$\alpha_s = \frac{R}{w}\frac{\partial w}{\partial n}$$

The key parameter is here α_s, which varies from $\alpha_s = -1$, i.e., potential flow (or free-vortex) spanwise velocity distribution with maximum velocity at the inner side, to $\alpha_s = 1$, i.e., forced-vortex with maximum velocity at the outer side (Blanckaert and de Vriend, 2003; Ottevanger et al., 2012). The rationale is that, generally, $\alpha_s = -1$ at the bend entrance where the helical-flow production is stronger and the outward momentum transfer has still to affect the flow; as opposite, α_s tends to 1 as the high-velocity thread shifts to the outer side of the bend, i.e., where the vertical profile of velocity is likely to be flattened and the production of helical-flow weakened. Accordingly, the dampening factor f_D decreases for increasing α_s (Fig. 2b). Through the bend parameter β, f_D also depends on hydrodynamic variables (Y and R) and on bottom friction (m). For increasingly sharp bends, f_D decreases, indicating that non-linear effects become increasingly important in limiting the growth of helical flow.

The non-linear model by Blanckaert and de Vriend (2003) has been conceived for reduced order models developed on curvilinear reference frames, typically used as meander-migration models, in which the secondary currents are parameterized based on momentum balance at the channel centreline. Ottevanger (2013) proposed to extend the model to the whole channel width by extending the secondary flow intensity estimated at the centreline modulated with empirical power-law weighting functions. Such an extension is limited to regular-shaped cross-sections and presumes the knowledge of the channel centreline and walls. Iterative procedures are required to deal with more complex geometries (Qin et al., 2019). The generalization of this nonlinear model to a form that is suitable to general-purpose 2D schemes is still to be sought.

2.4. A pure 2D approach and the treatment of banks

Within the scope of general-purpose 2D depth-averaged models, which include the salient features of curvature-induced secondary flows, the approach used to account for impervious banks and the transversal distribution of the D_{sn} dispersive stress deserves some discussions.

As well explained by Blanckaert (2001), it is known since Johannesson and Parker (1989a) that, in a channel bend, the D_{sn} dispersive stress must satisfy two conditions: *i*) it should be positive in the central region of the cross section, where the helical flow produces the highest transversal momentum flux, and *ii*) it should decay to zero toward the impervious banks, where the direction of secondary flow is mostly vertical and the velocity progressively reduces due to sidewall friction. When applying linear models for secondary currents to strongly curved flows, the helical flow intensity is generally overestimated when the (physically sound) hypotheses of no-slip condition is assumed (e.g., Blanckaert, 2001; Lien et al., 1999). Indeed, in the external part of the bend, the no-slip condition amplifies the (negative outward) spanwise gradient of velocity, entailing a larger, streamwise-oriented, net stress at the outer side of the bend.

A simple solution that has often been used in previous studies (Lien et al., 1999; Song et al., 2012) is adopting the free-slip condition at impervious banks. The spanwise gradient of velocity is reduced, and so it is the dispersive stress D_{sn}; unfortunately, this causes an unphysical momentum flux at the banks (Johannesson and Parker, 1989a). Moreover, while assuming a free-slip condition at the banks entails minor drawbacks in case of relatively large cross-sections, the sidewall friction plays a significant role in case of cross-sections with large aspect ratios, typical of artificial channels and laboratory flumes, and should be accounted for.

Physics-based analytical solutions proposed in previous studies (e.g., Ikeda et al., 1990) are unsuitable to general-purpose 2D depth-averaged models, for which the channel centreline and width, as well as the distance from the banks, cannot even be identified. Actually, the bank location can change substantially depending on the water level in typical compound cross-sections (e.g., passing from full-bank to flood discharge), as well as due to movable-bed dynamics in case of active (i.e., migrating, braided, anabranching) riverbeds.

In general-purpose 2D models based on a Cartesian (i.e., not curvilinear) reference frame, only local variables (i.e., the flow depth and velocity, the radius of curvature R, etc.) can be used to estimate the helical flow strength (Jin and Steffler, 1993; Koch and Flokstra, 1980). Hence, here we explore the practical solution of implementing a model for secondary flow, including the associated non-linear saturation effects, based on local variables only. The effectiveness of such a pure 2D approach has to be verified by means of model applications (the reader is referred to Sect. 3 and 4). The basic idea is that considering the physics-based saturation effects, rather than the unphysical free-slip condition at sidewalls or other case-specific tuning parameters, could alleviate the overestimation of secondary flow that is produced in strongly curved bends when the no-slip condition acts at impervious banks.

Of course, providing a physically sound representation of the complex 3D phenomena occurring in strongly curved channel bends is beyond the scope of the present work. The goal is achieving a cost-effective, versatile, and useful tools for engineering applications.

2.5. Advection-diffusion equation in the presence of secondary currents

The advection-diffusion equation allows to determine the evolution in time and space of the vertically-averaged concentration, C, of tracers and substances transported by the flow. It is used to model suspended sediment, pollutant transport, and other transported quantities such as the vorticity ω (Sect. 2.2). The advection-diffusion equation can be

written as:

$$\frac{\partial YC}{\partial t} + \nabla\cdot C\mathbf{q} - \nabla\cdot(\varepsilon_T \nabla C) - \nabla\cdot(Y\mathbf{D_D}\nabla C) = S \tag{13}$$

where $\nabla\cdot$ is the 2D divergence operator, $\varepsilon_T = \nu_T / \sigma_T$ is the turbulent diffusivity, commonly expressed as a function of the eddy viscosity, ν_T, and of the Schmidt number, σ_T (Duan, 2004), $\mathbf{D_D}$ is an anisotropic diffusivity tensor that accounts for dispersion, and S is a source term.

The dispersive-diffusion term is often neglected in the practice (i.e., $\mathbf{D_D} = 0$), and the turbulent diffusivity is tuned using the Schmidt-number as a calibration parameter for representing experimental data in general conditions (smaller values for the Schmidt number increase the mixing and vice-versa) (Duan, 2004; Hu et al., 2017). However, the curvature-induced helical flow enhances the lateral mixing (Engmann, 1986; Fischer, 1969; Lee and Kim, 2012; Moncho-Esteve et al., 2017; Rishnappan and Lau, 1977). Particularly, large curvature and strong secondary currents entail a marked anisotropic diffusivity that needs to be modelled with a suitable parameterization (Demuren and Rodi, 1986; Duan, 2004). This generally suffices to make the calibration of the Schmidt number unnecessary (i.e., $\sigma_T = 1$ can be assumed) in the case of channel bends.

The principal components of the $\mathbf{D_D}$ tensor, in the local (s, n) reference frame, can be expressed in the following general form:

$$D_{Dss} = \alpha_{Ds} u_* Y \qquad D_{Dnn} = \alpha_{Dn} u_* Y \qquad D_{Dsn} = D_{Dns} = 0 \tag{14}$$

where u_* is the friction velocity and α_{Ds}, α_{Dn} are proper parameters Elder, 1959; Holly and Usseglio-Polatera, 1984; Shin et al., 2020). Different formulations for α_{Ds} and α_{Dn} are available in the literature, depending on flow and environmental conditions, e.g., the shape of the velocity profile (Seo and Baek, 2004) or the presence of vegetation (Lou et al., 2020). Following Elder (1959), a common choice is $\alpha_{Ds} = 5.93$. To account for the presence of helical flows, α_{Dn} can be estimated as a function of the transversal velocity at the free-surface, v_{ns}, as a result of depth-averaging (Fischer et al., 1979; Lee and Seo, 2013). Considering the vertical distributions of velocity expressed by Eqs. (4) and ((5) leads to

$$\alpha_{Dn} = \frac{1}{6\kappa}\left(\frac{v_{ns}}{u_*}\right)^2 \tag{15}$$

Finally, by rotating the principal-component tensor onto the (x, y) reference frame, the diffusivity components D_{Dij} become (Alavian, 1986):

$$\begin{aligned} D_{Dxx} &= D_{Dss}\frac{u^2}{w^2} + D_{Dnn}\frac{v^2}{w^2} \\ D_{Dxy} &= D_{Dyx} = (D_{Dss} - D_{Dnn})\frac{uv}{w^2} \\ D_{Dyy} &= D_{Dss}\frac{v^2}{w^2} + D_{Dnn}\frac{u^2}{w^2} \end{aligned} \tag{16}$$

2.6. The 2DEF finite element numerical model

The different parameterizations of curvature-induced secondary currents are implemented in the framework of the 2DEF Finite Element hydrodynamic model (D'Alpaos and Defina, 2007; Defina, 2003; Viero et al., 2014; 2013). The model solves Eqs. (1), which constitute a modified version of the full shallow water equations, to deal with wetting and drying processes over irregular topography (Defina, 2000). The bottom friction is expressed using the Strickler-Manning formulation; it is treated semi-implicitly to enhance model stability (Cea and Bladé, 2015; Valiani et al., 2002; Viero and Valipour, 2017).

The computational domain is discretized with 2D triangular elements. A staggered scheme is used in which water levels are defined at the grid nodes and assumed to vary piecewise linearly through the domain; flat triangular elements, characterized by a constant elevation, convey the discharge among adjacent nodes. In the framework of semi-implicit, mixed Eulerian-Lagrangian scheme, in the momentum equation the material (Lagrangian) derivative of the depth-averaged velocity is replaced by its finite difference formulation:

$$\frac{\mathrm{D}\mathbf{w}}{\mathrm{D}t} = \frac{\mathbf{w} - \mathbf{w}_0}{\Delta t} \tag{17}$$

where the subscript "0″ indicates the terms at the previous time step and position (backward along the Lagrangian trajectory). Under the hypothesis of slowly varying flows, momentum equations are linearized and then solved for $\mathbf{q} = \mathbf{w}Y$, which in turn are substituted into the continuity equation, and solved with a Finite Element Galerkin's method (Defina, 2003). The semi-implicit nature of the scheme limits its applicability to subcritical flows, yet relaxes the CFL restriction on the computational time step. A single system of N algebraic equations, being N the number of nodes, is solved at each time step by a modified conjugate gradient method. Considering that the accuracy of the scheme allows for using relatively coarse meshes, the model turns out to be particularly efficient.

2.6.1. Computation of the local streamline curvature

The Lagrangian approach for convective terms is used also to estimate the local radius of curvature of the streamlines, based on the spatial variation of the direction of the velocity (Bonetto and Defina, 1998). Denoting with ϑ the angle of the velocity vector to the x axis (positive counter clockwise) and with R the local radius of curvature of the streamline (Fig. 1b), the streamwise distance ds can be written as:

$$ds = -R\,[\vartheta(s+ds) - \vartheta(s)] = -R\,d\vartheta \tag{18}$$

Observing that $\tan\vartheta = v/u$ and $\cos\vartheta = u/w$, the derivative of ϑ can be expressed in terms of velocity components as:

$$\frac{d}{ds}\left(\frac{v}{u}\right) = \frac{d}{ds}\tan\theta = \frac{1}{\cos^2\vartheta}\frac{d\vartheta}{ds} = \left(\frac{w}{u}\right)^2\frac{d\vartheta}{ds} \tag{19}$$

The local streamline curvature, $1/R$, is then obtained by combining Eqs. (18) and (19):

$$\frac{1}{R} = -\frac{d\vartheta}{ds} = -\left(\frac{u}{w}\right)^2\frac{d}{ds}\left(\frac{v}{u}\right) = -\frac{u^2}{w^2}\left(\frac{1}{u}\frac{dv}{ds} - \frac{v}{u^2}\frac{du}{ds}\right) = \frac{1}{w^2}\left(v\frac{du}{ds} - u\frac{dv}{ds}\right) \tag{20}$$

For slowly varying flows, $\Delta s \cong w_1 \Delta t$, and the spatial derivative of the velocity components can be approximated as:

$$\frac{du}{ds}\Big|_1 \cong \frac{u_1 - u_0}{w_1\Delta t};\quad \frac{dv}{ds}\Big|_1 \cong \frac{v_1 - v_0}{w_1\Delta t} \tag{21}$$

where the label "1″ denotes the centre of a generic cell. Hence, making use of Eqs. (20) and (21), the local curvature is finally given by:

$$\frac{1}{R_1} \cong \frac{1}{w_1^3\Delta t}[v_1(u_1 - u_0) - u_1(v_1 - v_0)] = \frac{1}{w_1^3\Delta t}[u_1\ v_0 - v_1 u_0] \tag{22}$$

2.6.2. Computation of the Reynolds turbulent stresses

The horizontal components of Reynolds turbulent stresses are modelled with the Boussinesq approximation and the depth integrated eddy viscosity by Stansby (2003) and Uittenbogaard and van Vossen (2004) (see also Viero, 2019). The Reynolds terms in Eqs. (1) are

$$Re_{ij} \cong \nu_T Y\left(\frac{\partial u_i}{\partial j} + \frac{\partial u_j}{\partial i}\right) \tag{23}$$

with indexes i and j denoting either x or y, ν_T the eddy viscosity, and $u_i = q_i/Y$ the generic depth-averaged velocity component. Looking at the first equation in (1), under the hypothesis of smooth spatial variations of the eddy viscosity, the first Reynolds stress component becomes

$$\frac{\partial Re_{xx}}{\partial x}+\frac{\partial Re_{xy}}{\partial y} \cong \nu_T Y\left[\frac{\partial}{\partial x}\left(2\frac{\partial u_x}{\partial x}\right)+\frac{\partial}{\partial y}\left(\frac{\partial u_x}{\partial y}+\frac{\partial u_y}{\partial x}\right)\right] = \\ = \nu_T Y\left(\frac{\partial^2 u_x}{\partial x^2}+\frac{\partial^2 u_x}{\partial y^2}\right)+\nu_T Y\frac{\partial}{\partial x}\left(\frac{\partial u_x}{\partial x}+\frac{\partial u_y}{\partial y}\right) \tag{24}$$

According to the continuity equation in (1), the last right-hand side term is proportional to the temporal variation of the water level, and is negligible in case of slowly varying flows. Hence, the Reynolds stress can be estimated as

$$\begin{bmatrix}\frac{\partial Re_{xx}}{\partial x}+\frac{\partial Re_{xy}}{\partial y}\\ \frac{\partial Re_{yx}}{\partial x}+\frac{\partial Re_{yy}}{\partial y}\end{bmatrix} \cong \nu_T Y\begin{bmatrix}\frac{\partial^2 u_x}{\partial x^2}+\frac{\partial^2 u_x}{\partial y^2}\\ \frac{\partial^2 u_y}{\partial x^2}+\frac{\partial^2 u_y}{\partial y^2}\end{bmatrix} = \nu_T Y\nabla^2\mathbf{u} \tag{25}$$

Considering that these terms have to be computed for each element of an unstructured triangular mesh, the divergence theorem is used to obtain the average cell value of the Reynolds stresses:

$$\frac{\nu_T Y}{A_e}\int_{A_e}\nabla^2\mathbf{u}\,dA = \frac{\nu_T Y}{A_e}\int_{\Gamma_e}\nabla\mathbf{u}\cdot\mathbf{n}_\Gamma\,d\Gamma \approx \frac{\nu_T Y}{A_e}\sum_k \nabla\mathbf{u}_k\cdot\mathbf{n}_k\,L_k \tag{26}$$

in which A_e is the area and Γ_e the boundary of the computational element, $\mathbf{n}_\Gamma$ is the unit-vector normal to the cell boundary (positive outward), and k identifies each of the three cell sides, whose length is L_k.

Denoting with O the centroid of the cell and with O_k the centroid of the cell adjacent to the k-th side of the cell, and with d_k the projection of the segment $\overline{OO_k}$ onto $\mathbf{n}_k$, the last term of Eq. (26) becomes

$$\frac{2\nu_T}{A_e}\sum_k(\mathbf{u}_{Ok}-\mathbf{u}_O)\frac{p_k L_k}{d_k} \tag{27}$$

in which the weight $p_k = \min(Y_k/Y;\,1)$ accounts for the fact that the Reynolds stresses take only place at the wet interface shared by adjacent cells (e.g., if the adjacent cell is dry, no Reynolds stress occurs). For cell sides belonging to the mesh boundary, assuming $\mathbf{u}_{Ok} = \mathbf{u}_O$ (or, equivalently, $p_k = 0$) allows simulating the slip-condition.

2.6.3. Computation of the dispersive stress terms

Similar to the Reynolds stresses, the computation of dispersive stresses in Eqs. (1) requires a suitable evaluation of the spatial derivatives of the D_{ij} terms defined at Eq. (7). Denoted the dispersive terms with

$$\mathbf{D} = \begin{bmatrix}D_{xx} & D_{xy}\\ D_{yx} & D_{yy}\end{bmatrix} \tag{28}$$

the dispersive stresses are given by $\nabla\cdot\mathbf{D}$. The average of the dispersive stresses for each computational cell can be evaluated making use of the divergence of $\mathbf{D}$:

$$\frac{1}{A_e}\int_{A_e}\nabla\cdot\mathbf{D}\,dA = \frac{1}{A_e}\int_{\Gamma_e}\mathbf{D}\cdot\mathbf{n}_\Gamma\,d\Gamma \approx \frac{1}{A_e}\sum_k\mathbf{D}_k\cdot\mathbf{n}_k\,L_k \tag{29}$$

in which $\mathbf{D}_k$ is the tensor of dispersive terms evaluated at the centre of the k-th cell side. This can be obtained as the average of the $\mathbf{D}$ terms, previously computed for adjacent cells and weighted with the distance of centroids to the centre of the k-th cell side.

Concerning the dampening factor, which accounts for the saturation of secondary flow in case of sharp bends, the key point is the computation of the transversal gradient of the velocity, which appears in Eq. (12) within α_s, and is equal to $\partial w/\partial n = \nabla w\bullet\mathbf{n}$, with $\mathbf{n}$ the unit vector normal to the local flow direction. Making use of the divergence theorem, for each computational cell the average value of the velocity gradient is evaluated as

$$\frac{1}{A_e}\int_{A_e}\nabla w\,dA = \frac{1}{A_e}\int_{\Gamma_e}w\mathbf{n}_\Gamma\,d\Gamma \approx \frac{1}{A_e}\sum_k w_k\,\mathbf{n}_{\Gamma k}\,L_k \tag{30}$$

where the velocity at the side centre, w_k, is computed as the average of the w at adjacent cells weighted with the distance of centroids to the centre of the k-th cell side, L_k is the length of the k-th cell side, and $\mathbf{n}_{\Gamma k}$ is the outward unit vector normal to the cell side.

2.6.4. Wall function to account for no-slip condition at sidewalls

At the mesh boundaries, the model allows imposing a classical slip condition, or to use a wall function to account for additional friction exerted by sidewalls. In the latter case, an additional stress component, parallel to the wall direction, is added to the momentum balance of wall-adjacent elements. It is computed as (Wu et al., 2000):

$$\tau_{wall} = \rho w^2\left[\frac{\kappa}{\ln\left(\frac{d_{wall}}{e_s}\right)}\right]^2 \tag{31}$$

where e_s is the equivalent sand grain roughness of lateral walls and d_{wall} is the limit between the buffer and the logarithmic layers at the wall (see Fig. 1c), assumed equal to

$$d_{wall} = \frac{50\,\nu}{u^*} \tag{32}$$

where ν is the kinematic viscosity of water, and u^* the shear velocity. For each grid cell, the wall shear stress is applied on the surface $Y\cdot b_{wall}$, being b_{wall} the length of the vertical wall.

2.6.5. Numerical scheme for the transport-diffusion equation

The transport-diffusion equation (Sect. 2.5) is solved using a conservative, second-order in space numerical scheme. The scheme is equivalent to that described by Casulli and Zanolli (2005), with the substantial difference that variables are located oppositely in the two staggered meshes. In Casulli and Zanolli (2005), the model cells are control volumes that exchange fluxes through the cell-sides; in the present model, the triangular elements convey fluxes from a node to the others, or from two nodes to the remaining one. The second order accuracy in space, for the advective terms, is achieved using an upwind, total variation diminishing (TVD) scheme; to avoid spurious oscillations, the SUPERBEE limiter is applied based on two consecutive gradients of nodal tracer concentration. For each node of the grid, the preliminary step is computing the upstream concentration as the average concentration of all the upstream nodes, weighted with the value of incoming water discharge (Casulli and Zanolli, 2005). Then, for each element, the direction of the velocity vector determines each couple of nodes that exchange flow and tracer with each other, and the concentration value at these two connected nodes is completed with the upstream concentration. The two consecutive gradients allow applying the TVD limiter, and the limited gradient of concentration is finally used to compute the tracer flux between nodes.

2.6.6. Bedload transport

The bed evolution module of the 2DEF model, described in Defina (2003), is based on the Exner sediment balance equation:

$$(1-n)\frac{\partial z_b}{\partial t}+\nabla\cdot\mathbf{q}_\mathbf{b} = 0 \tag{33}$$

where n is the bed sediment porosity, z_b the bottom elevation, and $\mathbf{q}_\mathbf{b}$ the volumetric sediment transport rate per unit width, expressed as (Struiksma, 1985):

$$|\mathbf{q}_\mathbf{b}| = q_{b0}\left(1-\chi c_f\frac{\partial z_b}{\partial s}\right) \tag{34}$$

being χ an empirical factor to account for the effect of longitudinal slope on transport rate ($\chi = 0.03$ according to Crosato and Struiksma, 1989) and c_f the friction coefficient ($c_f = K_S^2 Y^{4/3}/g$). The sediment transport rate, q_{b0}, is evaluated with a continuous variant (Carniello et al., 2012) of the threshold-based Meyer-Peter and Müller (MPM) formula:

$$q_{b0} = 8\sqrt{g d_s^3 (s-1)}\; T^{1.5} \text{ with } T = -\theta_C + \sqrt[4]{\theta_C^4 + \mu\theta^4} \tag{35}$$

where d_s is the characteristic (median) sediment diameter, $s = \rho_s/\rho$ the relative density of sediments, μ the ripple factor (Vermeer, 1986), θ the Shields parameter, and θ_C the threshold value for incipient bedload transport. Compared to the original MPM formulation, the continuous variant provides smoother (hence more stable), practically equivalent solutions.

The components of the sediment rate, q_{bx} and q_{by}, are obtained from $|\mathbf{q_b}|$ as a function the direction of sediment transport, which in turn depends on the near-bed flow velocity. In channel bends and meandering rivers, using the mean velocity of the primary flow to estimate the bedload transport is often incorrect since the curvature-induced secondary flow can significantly affect the flow (and sediment) direction at the bottom (Abad et al., 2008; Kitanidis and Kennedy, 1984). The inward-oriented velocity at the bottom is the main cause of bend scour and of point-bar accretion, respectively at the outer and at the inner sides of bends (Bathurst et al., 1977; Engel and Rhoads, 2012; Rozovskii, 1957).

Empirical corrections have been proposed in the literature for representing the deviation of bedload transport to the mean flow velocity. Olesen (1987) suggested the following angular correction:

$$\Delta\beta = A_c \frac{Y}{R} \tag{36}$$

where A_c is a parameter typically assumed in the range $7 \div 12$. Accordingly, the bottom velocity can be estimated as:

$$\mathbf{w}_b = (u + \Delta\beta \cdot v; v - \Delta\beta \cdot u) \tag{37}$$

Such an approach still finds widespread applications in hydromorphological models (Vanzo et al., 2021). Yet, a major limitation comes from the direct dependence on the local streamline curvature, as in the instantaneous-adaptation approach for secondary flows (Sect. 2.2), which may produce unphysical results in case of large curvatures (inertia and saturation are not considered). Moreover, the bottom characteristics, such as the bed roughness that shapes the vertical profile of flow velocity, are not accounted for explicitly. As a consequence, such a correction model needs, at least, robust and site-specific calibration.

Alternatively, when curvature-induced helical flow is modelled effectively, the bottom deviation angle $\Delta\beta$ can be evaluated depending on the near-bed transversal velocity component. This is expected to provide a more accurate estimation of bedload than using empirical, local corrections (Wang and Tassi, 2014), as inertia, saturation, and vertical velocity profiles can be all accounted for. According to the linear velocity profile of Eq. (5), the transversal velocity component at the bottom is opposite to that at the free-surface, i.e., $-v_{ns}$. The near-bed velocity becomes equal to

$$\mathbf{w}_b = (u_b; v_b) = \left(u + v_{ns}^* \cdot v; v - v_{ns}^* \cdot u\right) \tag{38}$$

and it forms an angle $\delta = \arctan(v_b/u_b)$ to the x axis. The direction of sediment transport, α, is also influenced by the bed slope (Baar et al., 2018; Chavarrías et al., 2019), which is accounted for according to Struiksma (1985):

$$\alpha = \arctan\left[\frac{\text{sen}(\delta) - \frac{1}{f(\theta)}\frac{\partial z_b}{\partial y}}{\cos(\delta) - \frac{1}{f(\theta)}\frac{\partial z_b}{\partial x}}\right] \tag{39}$$

The function $f(\theta)$ weights the influence of the transverse bed slope and is estimated as (Talmon et al., 1995):

$$f(\theta) = \zeta \cdot \sqrt{\theta} \text{ with } \zeta = 9(d_s/Y)^{0.3} \tag{40}$$

3. Results

3.1. Test with fixed-bed, mild-curvature, laboratory experiments

The effectiveness of secondary flow parameterizations described in the previous section is first verified by comparing the hydrodynamic field, modelled with different approaches, to the laboratory data from the RIPRAP test facility experiment (Bernard and Schneider, 1992; Finnie et al., 1999).The RIPRAP channel is $L = 274$ m long and $B = 5.27$ m wide, with 2:1 bank slope in the lower part of lateral walls (Fig. 3). The four bends (90° and 135° right wise, 90° left wise and 135° right wise) have a constant centreline radius of curvature $R = 15.2$ m. The longitudinal slope is 0.216% and the Strickler roughness coefficient is $K_S = 38.5\ \text{m}^{1/3}/\text{s}$.

The numerical mesh is made of 6,293 nodes and 11,528 triangles, with mean linear size of 45 cm (i.e., channel width to cell-side-length ratio, $B/\Delta x$, of about 12). The model of Odgaard (1986) is used for the source terms in Eq. (10) and (11) (see also Table 1), and the wall function of Eq. (31) is used to enforce the no-slip condition at the lateral boundaries, thus accounting for the presence of side walls. As boundary conditions, constant flowrate ($Q = 4.25\ \text{m}^3/\text{s}$) and water depth ($Y_D = 0.8$ m) are imposed at the inlet and outlet sections, respectively.

Fig. 4 shows the spanwise profiles of depth-averaged velocity, in steady state conditions, for the 11 cross-sections of Figure 3; the experimental data (red dots, from Finnie et al., 1999) are compared with model results obtained without considering dispersive stresses (dotted lines), with the instantaneous-adaptation (solid lines), and with the vorticity transport (dash-dotted lines) approaches. For the same cases, the plan view of Fig. 5 shows the location of the main stream (high-velocity thread). In the Supplementary Material, Figure S1 highlights the importance of using a wall function to account for the resistance induced by sidewalls, and Figure S2 and S3 the performance of the different formulations, collected in Table 1, for the source terms of Eq. (10) and (11).

Fig. 4 confirms that accounting for curvature-induced secondary flow is necessary to obtain reasonable transversal velocity profiles in the presence of bends. While the difference with a classical 2D formulation without dispersive terms is striking, the local instantaneous-adaptation and the vorticity-transport approaches perform similarly to each other; they both reproduce the experimental data very well, with the vorticity-transport approach slightly retarding the development of the secondary flow, and in turn the outer shift of higher velocities, at the beginning of bends (see Sect. 2, 6, and 10). The mean RMSE evaluated for the whole 11 sections is 0.224 m/s without dispersive terms, 0.109 m/s using the local approach, and 0.123 m/s using the vorticity-

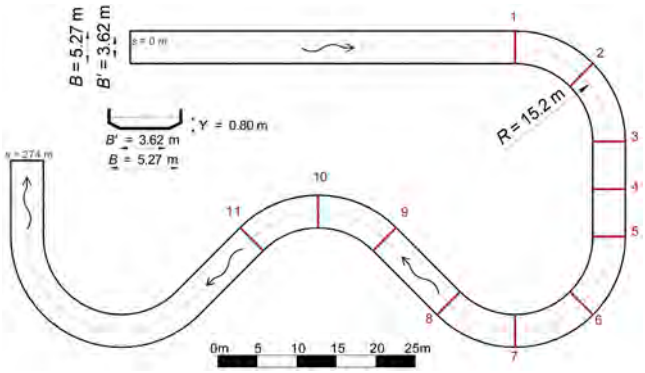

Fig. 3. The RIPRAP facility channel (Finnie et al., 1999) with numbered cross-sections.

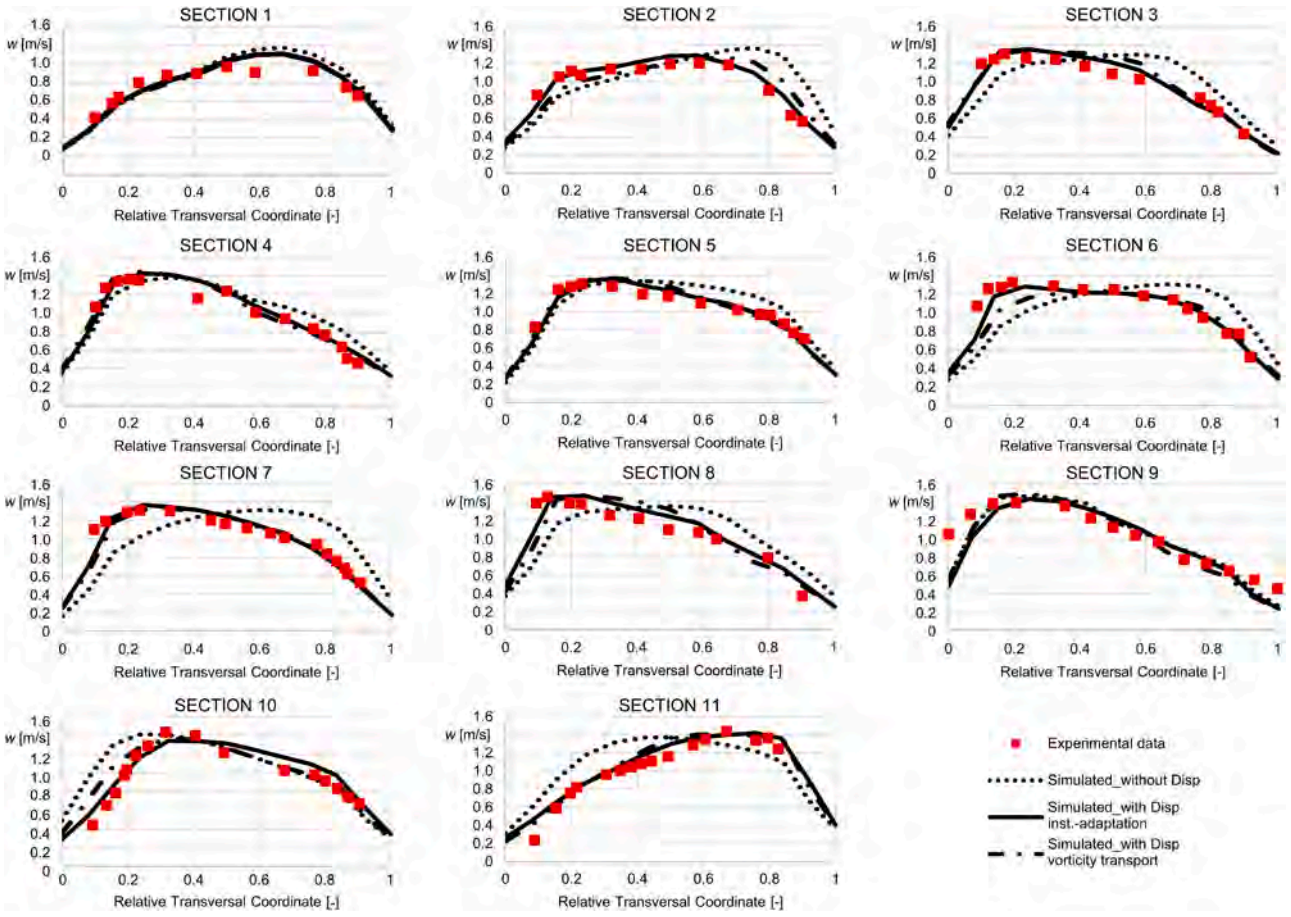

Fig. 4. Transversal profiles of depth-averaged velocity in the RIPRAP test (Finnie et al., 1999): measured data (red dots) and modelled profiles without dispersive terms (dotted lines), with the instantaneous-adaptation approach (solid lines) and with the vorticity-transport approach (dash-dotted lines). The relative transversal coordinate spans the channel width from the left bank.

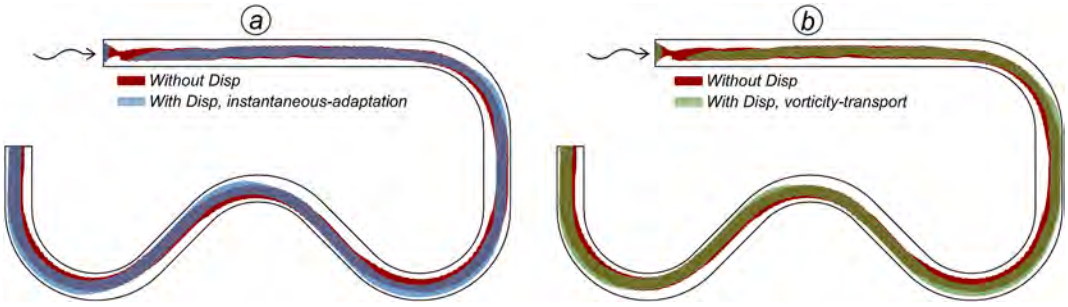

Fig. 5. Main stream flow (velocity higher than 1.15 m/s) for the model without the dispersive terms (red) and a) with the instantaneous-adaptation approach (blue), b) with the vorticity-transport approach (green) for curvature-induced secondary flow.

transport approach.

The dispersive stresses in the SWEs produce deceleration of the flow in the inner part and acceleration at the outer part of the bend (Dietrich and Smith, 1983), thus shifting the high-velocity thread toward the outer side of bends compared to the simulation without dispersive terms (Fig. 5). Fig. 5 also shows one of the main differences between the instantaneous-adaptation and the vorticity-transport approaches; by looking at the undisturbed flow approaching the first bend, the outward shift of the high-velocity thread is faster with the local approach (Fig. 5a), as it doesn't account for rotational inertia. On the contrary, the vorticity-transport approach can account for the phase lag, which becomes more important in the last part (and downstream) of bends. Indeed, the vorticity-transport approach (Fig. 5b) shows a persistent deviation of the high-velocity thread well after the bend (i.e., when there is no more curvature of the streamlines). In the case of multiple subsequent bends, the residual helical flow interacts with the secondary current that grows in the following bend (Abad and Garcia, 2009), thus increasing or decreasing the intensity of the helical flow depending on the curvature sign of successive bends. Passing from the first to the second bend, the high-velocity thread returns to the channel centre with the local approach, whereas it remains at the outer (left) side of the channel by transporting the vorticity. On the contrary, the change in curvature sign in the two last bends produces a retarded outward shift of the high-velocity thread in Fig. 5b.

In the RIPRAP experiment, the width ratio $Y/B \approx 0.2$ is quite low; notwithstanding, the sidewalls of the channel affect significantly the

transversal velocity profile. As shown in Figure S1 (Supplementary Material), without including a wall function for the boundary elements, the model overpredicts the flow velocity close to the walls, and at some sections this overprediction becomes larger when including the dispersive stresses for curvature-induced helical flow.

The different formulations implemented for the source terms k_P and k_D in Eq. (10) and (11), reported in Table 1, produce very similar results. The different solutions become nearly indistinguishable both using the instantaneous-adaptation and the vorticity-transport approach (Figures S2 and S3 in the Supplementary Material).

3.2. Test with fixed-bed, strong-curvature, laboratory experiments

In strongly curved bends, the strong secondary circulation produced by the large streamline curvature flattens the vertical profile of velocity, thus weakening the mechanism of helical-flow production in what is called the saturation of secondary flows (Blanckaert and de Vriend, 2003). We use the experiments of Blanckaert and de Vriend (2003) and Rozovskii (1957), in which the curvature is strong and the saturation effect plays a key role, to check the model accuracy in terms of secondary circulation strength and spatial pattern.

The Ecole Polytechnique Fédérale Lausanne (EPFL) channel (Blanckaert and de Vriend, 2003) has a length $L = 19.7$ m and a width $B = 1.3$ m, with vertical side walls. The bend develops for 193° with a constant curvature (radius $R = 1.7$ m at the centreline, Fig. 6a). For the experiment here considered, the bottom is flat and fixed, and the Strickler coefficient is $K_S = 60$ m$^{1/3}$/s. Three different steady-flow experiments have been conducted with inflow of 56, 89, and 104 l/s and downstream water depth of 10.9, 16.0, and 21.3 cm, respectively. With fixed upstream discharge and downstream water level, numerical simulations have been run until steady state conditions are attained. For the three scenarios, the bend sharpness is $Y/R = 0.065$, 0.095, and 0.125.

The dampening factor, f_D, introduced in Sects. 2.2 and 2.3, is computed for each computational cell based on the local flow variables, and in particular on the transversal gradient of longitudinal velocity, α_s. Fig. 7 shows that, in the first part of the bend, the high-velocity thread is located at the inner side of the bend ($\alpha_s < 0$ as in a potential flow), the streamise vorticity is still developing and the interaction with the primary flow is negligible: the production of streamwise vorticity is maximum ($f_D \approx 1$). In the second part of the bend, as the high-velocity thread is moved outward by the momentum transfer associated to the helical flow (α_s progressively increases), the non-linear saturation feedback mechanism becomes important and the production of vorticity is reduced ($f_D << 1$). At the downstream end of the bend, the high-velocity thread is close to the outer bank and $\alpha_s \approx 1$. Expectedly, by increasing the bend sharpness Y/R, the saturation effect develops faster and becomes stronger (second and third column in Fig. 7), with the consequence that the helical flow intensity does not grow much with Y/R.

In Fig. 8, the model results are compared with experimental data in terms of the non-dimensional quantity $\langle f_n^2 \rangle$ (angle brackets highlight depth-averaging), which measures the strength of the secondary circulation and is defined as (Blanckaert and de Vriend, 2003):

$$\langle f_n{}^2 \rangle = \frac{\langle v_{ns}^2 \rangle}{\left(\frac{wY}{R}\right)^2} \tag{41}$$

Comparing the results with experimental data, the non-linear model allows to predict the magnitude of the secondary flow far more precisely than the linear model, confirming the effectiveness of the present approach. It has to be said that, while $\langle f_n^2 \rangle$ magnifies the secondary flow strength (thus the difference between linear and non-linear models), the change in the flow field obtained by accounting for non-linear saturation model is quite small in the first case ($Q = 56$ l/s), and more important for the largest discharge values. This suggests that accounting for non-linear effects improves the model predictions, and becomes fundamental for larger values of the bends sharpness.

The channel used by Rozovskii (1957) has a length $L = 11.5$ m and a width $B = 0.8$ m, with vertical side walls. The bend develops for 180° with a constant curvature (radius $R = 0.8$ m at the centreline, Fig. 6b). For the experiment here considered, the bottom is flat and fixed, and the Strickler roughness coefficient is $K_S = 70$ m$^{1/3}$/s. The inlet velocity is $w = 0.26$ m/s, and the downstream water depth is $Y = 5.1$ cm. The bend sharpness is $Y/R \approx 0.07$.

The model results, obtained with the no-slip condition at the sidewalls, are compared with the measured data in terms of depth-averaged velocity at different cross-sections (Fig. 9), and in terms of water surface elevation along the channel at the inner and outer sidewalls (Fig. 10). The model without dispersive terms overpredicts the velocity peak at the inner part of the bend, as can be noted especially between Section 5 and 11 in Fig. 9. Introducing the dispersive terms with a linear formulation (i.e., $f_D = 1$ in Eq. (10) or in Eq. (11)), the high-velocity thread is shifted to the outer side of the bend (dash-dotted lines), overestimating the observed redistribution of velocity, especially in the final part of the bend. Including the representation of the saturation mechanisms leads to a general improvement of model predictions. The free-surface profiles in Fig. 10 show that a classical 2D model without dispersive terms tends to underpredict the head losses. The linear model for secondary currents leads to a significant overestimation of head losses, probably because the flow is much confinated toward the outer side of the bend. Again, including the non-linear effect improves the model prediction.

The interest here is checking the effectiveness of the pure 2D non-linear model for secondary flow in terms of transversal distribution of dispersive stresses, as discussed in Sect. 2.4. For the experiment by Blanckaert and de Vriend (2003) with a discharge of 89 l/s, Fig. 11a shows the spanwise distribution of the D_{sn} dispersive term at 90° from the beginning of the bend; the red line shows the measured data as reported by Ottevanger (2013). Linear models, either analytical (Ottevanger, 2013) or the present numerical scheme (green and black dash-dotted lines, respectively) overrate the dispersive stress, especially close to the sidewalls, where it has to decay to zero (Johannesson and Parker, 1989a; Blanckaert, 2001). The prediction from the non-linear model with the no-slip condition at sidewalls (black solid line) is in

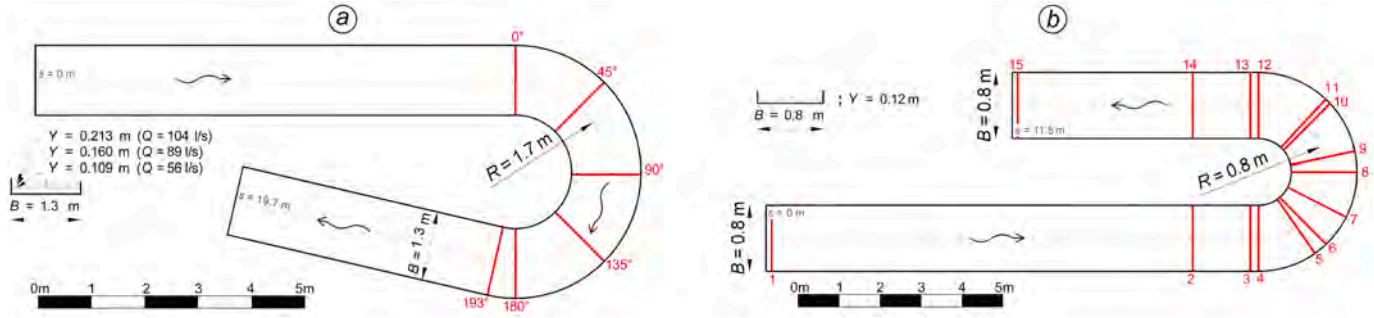

Fig. 6. a) The EPFL channel (Blanckaert and de Vriend, 2003), and b) the Rozovskii (1957) channel, with numbered cross-sections.

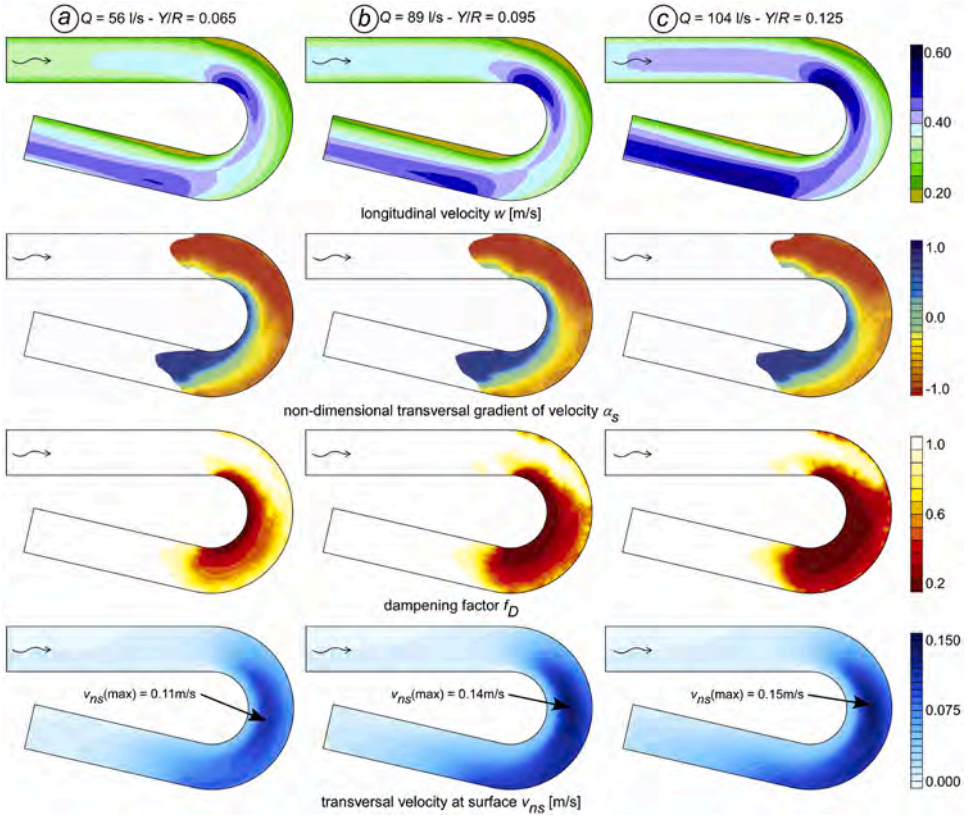

Fig. 7. Spatial distribution of the depth-averaged flow velocity, w, of the normalized transversal gradient of velocity, α_s, of the dampening factor, f_D, and of the transversal velocity at the free surface, v_{ns}, for a) $Q = 56$ l/s, b) $Q = 89$ l/s, and c) $Q = 104$ l/s. Note that the α_s field has been masked where the local curvature radius, R, is larger than 20 m (both R and α_s tend to infinity in straight reaches).

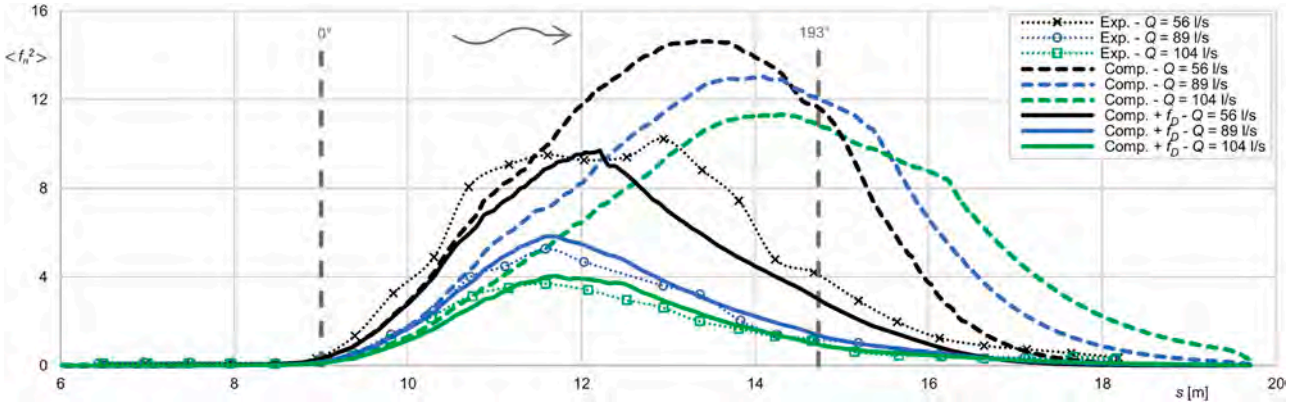

Fig. 8. Magnitude of the secondary current, $\langle f_n^2 \rangle$ along the EPFL channel bend axis. Comparison of experimental data (symbols, adapted from Blanckaert and de Vriend, 2003) with the results of the linear (dashed lines) and non-linear (solid lines) models, for the three discharge values considered in the experiments.

good agreement with the empirical formulation by Ottevanger (2013), and not too far from the measured data. A comparison among the same models and formulations, for the experiment by Rozovskii (1957), is reported in Fig. 11b in terms of transversal velocity at the free-surface, $-v_{ns}$, which stands for the helical flow intensity. Although measured data are not available, it emerges that *i*) linear formulations (dash-dotted lines) lead to excessively strong circulation, *ii*) the no-slip condition at the sidewalls reduces the momentum redistribution close to the banks (black lines), and *iii*) accounting for both the sidewall friction and the non-linear saturation effects (black solid line) improves the physical soundness of the solution.

3.3. Transport of passive tracers in curved channel

To test the model effectiveness in reproducing the transport of a generic passive tracer in presence of curvature-induced secondary currents, we use the experiments of Chang (1971), which have been subject to many model applications (see e.g., Begnudelli et al., 2010; Duan, 2004; Duan and Nanda, 2006; Ye and McCorquodale, 1997). The flume is 35.4 m long and it has two opposite 90° bends with a radius of curvature $R = 8.53$ m; the cross-section is rectangular and the width is $B = 2.34$ m. The mean velocity is $U = 0.367$ m/s and the water depth is $Y = 0.115$ m, which are obtained imposing an upstream inflow of 0.0988 m^3/s, a downstream water level of 0.115 m, and running the model until steady state conditions are attained. A constant inflow of a conservative

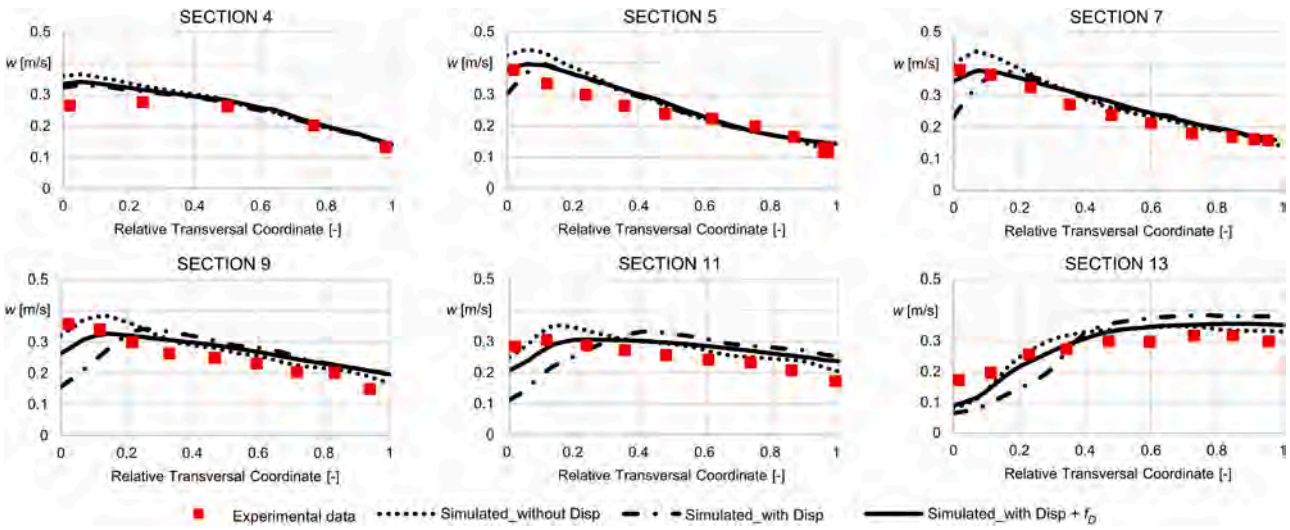

Fig. 9. Transversal profiles of depth-averaged velocity for the Rozovskii (1957) experiment (red squares), compared with model results without dispersive stresses (dotted lines), with the linear, instantaneous-adaptation approach (dash-dot lines), and with the non-linear model (solid line). The transversal coordinate spans the channel width from the left to the right bank.

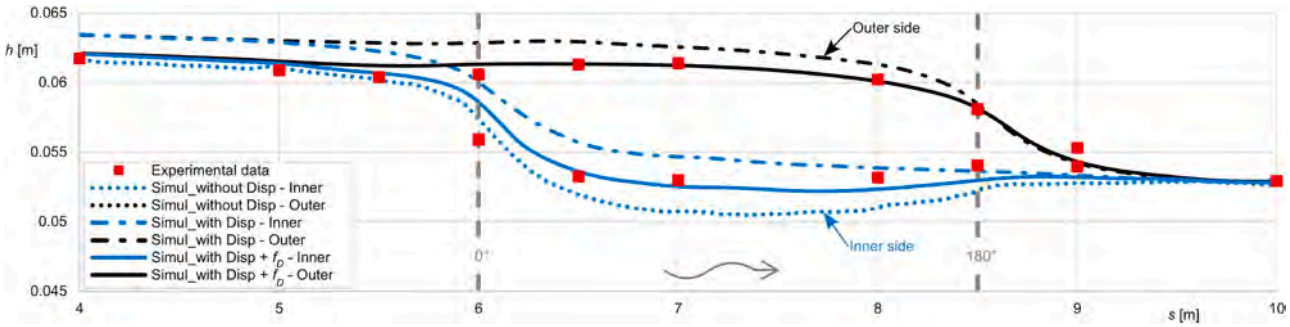

Fig. 10. Longitudinal profiles of water surface elevation at the outer (black lines) and inner (blue lines) sides of the bend. Red squares are the data measured by Rozovskii (1957); model results are shown without considering dispersive terms (dotted lines), with the linear model for secondary currents (dash-dot lines), and including the non-linear saturation effect (solid lines).

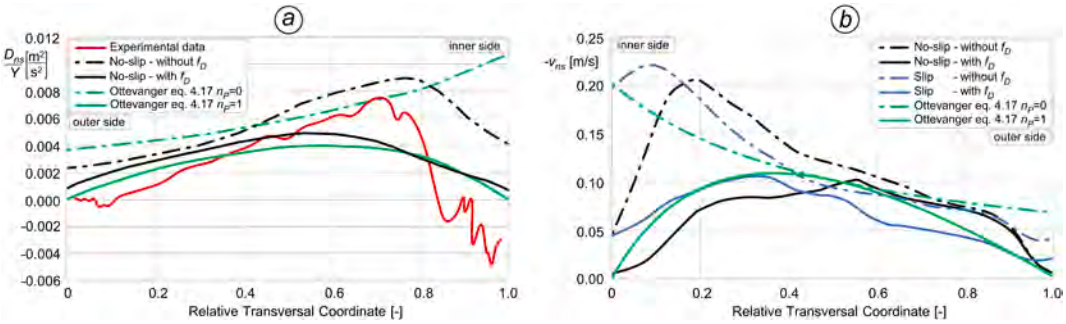

Fig. 11. a) Transversal profiles of the D_{ns}/Y dispersive term for the 89 l/s experiment by Blanckaert and de Vriend (2003) at 90° from the beginning of the bend. The red line resembles the experimental data reported by Ottevanger (2013). b) Transversal profiles of the helical flow intensity (in terms of $-v_{ns}$) for the Rozovskii (1957) experiment at cross-section 6. In both panels, dash-dotted lines denote linear formulations; for the present model, black and blue lines correspond to no-slip and free-slip condition at the sidewall, respectively; the green lines are the theoretical profiles from Ottevanger (2013), referring to a linear model and its power-law extension (dash-dotted and solid lines, respectively).

tracer ($Q_C = 0.01$ m^3/s) is then introduced as point injection located at 3 different transversal coordinates (the injection points are named IP$_1$, IP$_2$, and IP$_3$ in Fig. 12).

The mesh resolution is a key factor for controlling the numerical diffusion in transport problems (Begnudelli et al., 2010; Casulli and Zanolli, 2005). To test the mesh-dependency of the model solution, three different mesh grids have been used, with 3,396 (mesh 1x), 13,349 (mesh 4x), and 49,587 (mesh 16x) elements, respectively. These are obtained through halving the sides of each elements (i.e., the number of elements is about 4 times greater at each refinement). For the three meshes, the channel width to cell-side-length ratio, $B/\Delta x$, is about 10, 20, and 40. Figure S4 and Figure S5 in the Supplementary Material show that only the finest mesh (16x, channel width to cell-side-length ratio of about 40) leads to reliable results; with the coarser meshes (1x and 4x),

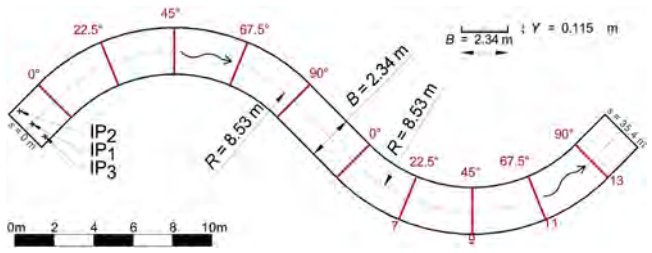

Fig. 12. Layout of the flume used in the experiments by Chang (1971), with the location of the three point injections (IP_1, IP_2, IP_3) considered in the experiments.

numerical diffusion becomes unacceptably high.

Using the finest mesh, the concentration profiles (Fig. 13) are in good agreement with the experimental data of Chang (1971). The comparison of solutions obtained with and without considering the curvature-induced dispersion (grey and black lines in Fig. 13) highlights the enhanced diffusion generated by the helical flow, well described introducing the dispersive terms in the transport-diffusion equation.

When a proper mesh resolution is used, the dispersive terms in the advection-diffusion equation allow reproducing the correct tracer distribution in the curved channel with the Schmidt number $\sigma_T = 1$. Contrarily, to match the experimental data without using these dispersive terms, the Schmidt number has to be tuned to lower values (Figure S6 of the Supplementary Material), so as to increase the spanwise diffusion artificially (Rodi, 2017; Ye and McCorquodale, 1998).

The top views of Fig. 14a,b, referring to the same scenarios of Fig. 13, suggest that the strength of the secondary flow is modest in the experiments of Chang (1971). This is confirmed by looking at Fig. 14c, d (lateral injection points IP_2 and IP_3): the tracer remains almost confined closed to the lateral walls, according to the experimental data and numerical results shown by Duan (2004) and Moncho-Esteve et al. (2017).

Finally, the role of the longitudinal dispersion terms (D_s in Eq. (14)) is highlighted in Figure S7 of the Supplementary Material by releasing the tracer at point IP_1 starting at $t = 0$, on a steady baseflow. With $D_s = 0$, the leading front of the "coloured" water reveals that the high-velocity thread is located at the inner side (free-vortex flow, weak velocity redistribution performed by the secondary current); the additional anisotropic, streamwise diffusion provided by the D_s terms makes the leading front faster and closer to the channel centreline.

3.4. Bedload transport – laboratory experiments

The parametrization of curvature-induced helical flows allows to estimate the near-bed transversal component of the flow velocity, thus predicting more precisely the direction of the bedload transport. To analyse this influence on the bed evolution, we considered the experiment performed by Koch and Flokstra (1980) at the Laboratory of Fluid Mechanics (LFM) channel. The channel has a rectangular cross-section (width $B = 1.7$ m) and a U-shape bend with curvature radius $R = 4.25$ m measured at the centreline. The longitudinal bed slope is 0.18% and the Strickler roughness coefficient is $K_S = 36\ m^{1/3}/s$. The discharge is $Q = 0.17\ m^3/s$ and the downstream water depth is $Y = 0.2$ m. The bed sediment has a median diameter $d_s = 0.78$ mm and a relative density $s = 2.65$.

The mesh has 1,719 nodes and 3,040 elements, corresponding to about 8 elements per channel width. The simulations started from a previously-computed steady flow over a bed with only streamwise slope; then, keeping fixed the inflow discharge and the downstream water level, the bed is left free to evolve until an equilibrium state is reached.

Without any corrections to account for helical flow, the bottom shear stresses are aligned to the primary flow (Fig. 15a). Introducing the secondary current correction, bottom stresses change their direction inward (Fig. 15b). This produces an imbalance in the bedload transport, with leads to scouring at the outer side and bed accretion at the inner part of the bend.

The bed topography at equilibrium is shown in the colour maps of Fig. 16 in terms of erosion/deposition with respect to the initially flat bed, Δz, and in the transversal profiles of bed elevations reported in Fig. 17 (see also Figure S8 of the Supplementary Material, which plots the difference between computed and measured values of Δz). With respect to the experimental data (Fig. 16a), a 2D model with no corrections for the bedload direction leads to completely unreliable results: only the accelerations and decelerations associated to the free-vortex flow field at the beginning and at the end of the bend produce some modifications of the bed (Fig. 16b). The empirical correction of bedload direction proposed by Olesen (1987), with $A_c = 10$ in Eq. (36), tends to overestimates both erosion and depositions (Fig. 16c); especially, as this correction is based on the local radius of curvature, scour and deposition start at the very beginning of the bend (no phase lag) and proceed uniformly along the bend (in the experiment scour and erosion slightly decrease). At 135°, the computed Δz is over 3 times larger than the measured one (Fig. 17).

The explicit parametrization of the secondary current and the correction of bedload direction proposed by Bernard and Schneider (1992) leads to better estimations; compared to the instantaneous-adaptation approach (Fig. 16d), the vorticity-transport approach in Fig. 16e correctly reproduces the initial phase lag and the increased scour at the end of the bend, close to the outer wall. The cross-sections in Fig. 17 show that the inclusion of secondary flow, according to Bernard and Schneider (1992), well reproduces the inner aggradation, whereas the outer scour is underestimated.

Finally, Fig. 18 shows a comparison of the scour/deposition produced by the three different models for secondary flow here implemented. The bed evolution is estimated using different parametrization for secondary currents intensity. Compared to Bernard and Schneider (1992), which is in good agreement with experimental data, the models of Kalkwijk and Booji (1986) and Odgaard (1986) slightly underestimate the magnitude of Δz, yet with a very similar spatial pattern (see also Figure S9 of the Supplementary Material, which plots the difference between computed and measured values of Δz).

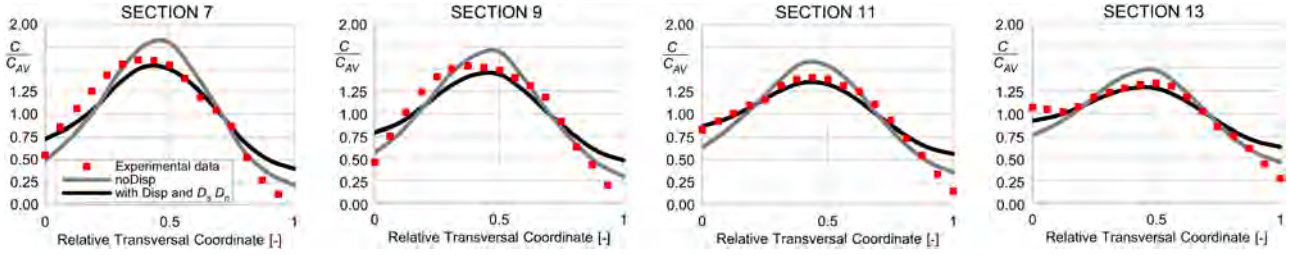

Fig. 13. For the Chang (1971) experiment with point injection IP_1 and for the finest mesh (16x), transversal profiles of relative concentrations for Sections 7, 9, 11, and 13: experimental data (red dots) and model results without (grey lines) and with (black lines) dispersive terms in the momentum advection-diffusion equations.

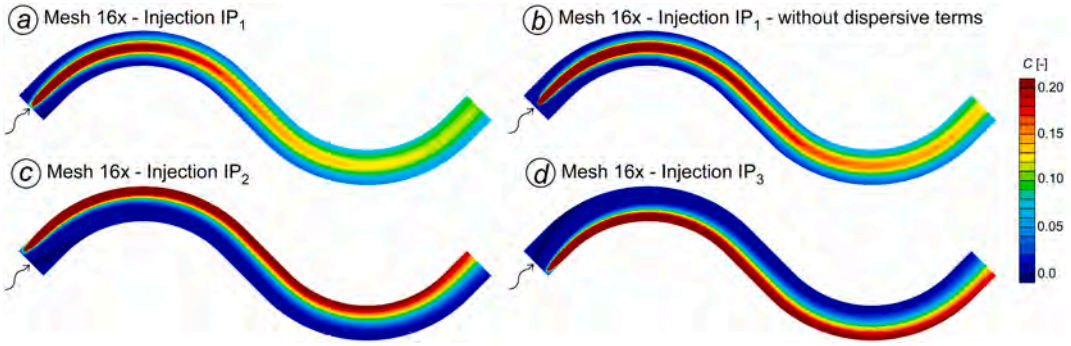

Fig. 14. For the Chang (1971) experiment, depth-averaged normalized concentration obtained with the finer mesh 16x. For IP_1, with (a) and without (b) dispersive terms in the momentum and transport-diffusion equations; for IP_2 (c) and IP_3 (d) with dispersive terms.

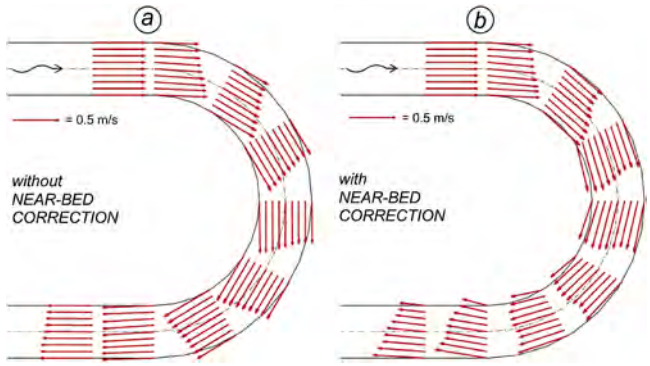

Fig. 15. Water velocity vectors at the bottom without (a) and with (b) correction for the secondary flow.

3.5. Real-world case study: fixed and mobile bed

The model is finally applied to a real-world case study, the ~50 km long reach of the Po River (Northern Italy) between the Mincio and the Panaro confluences, i.e., from 12 km upstream of Ostiglia to 8 km downstream of Ficarolo (Fig. 19). The meandering reach has been modelled using a 2D triangular grid with 58,570 nodes and 114,452 elements. The focus is here on three meandering bends, denoted as M1, M2, and M3 in Fig. 19. Table 2 reports additional details. The bathymetry, derived from a 2004 multibeam survey merged with a 2008 LiDAR survey, is shown in Figure S10 of the Supplementary Material.

A fixed water level, derived from an available rating curve, is used as downstream boundary condition. We then considered three different discharge scenarios, named Q_3990, Q_7400, Q_11,500 (where Q denotes the discharge expressed in m^3/s and imposed at the inlet section).

For each discharge scenario, a first set of simulations has been performed with the fixed, real bathymetry, with and without including the dispersive terms in the momentum equations. The inclusion of secondary flow correction entails minor changes to the flow field. An example is shown in Figure 20; at the AA cross-section (meander M1), the increase and the outer shift of the peak velocity, obtained by including the correction for the secondary flow, is absolutely modest, and it further decreases for lower flowrate values (e.g., $Q = 3990$ m^3/s, Fig. 20b). Using the instantaneous adaptation or the vorticity-transport approach entails negligible differences as well (dashed and solid lines in Fig. 20b). Similar results are obtained for meanders M2 and M3 (some relevant parameters are reported in Table 2). The depth-averaged velocity field at meander M1, for the discharge $Q = 11{,}500$ m^3/s and including the dispersive stresses in the momentum equations, is shown in Fig. 21. The

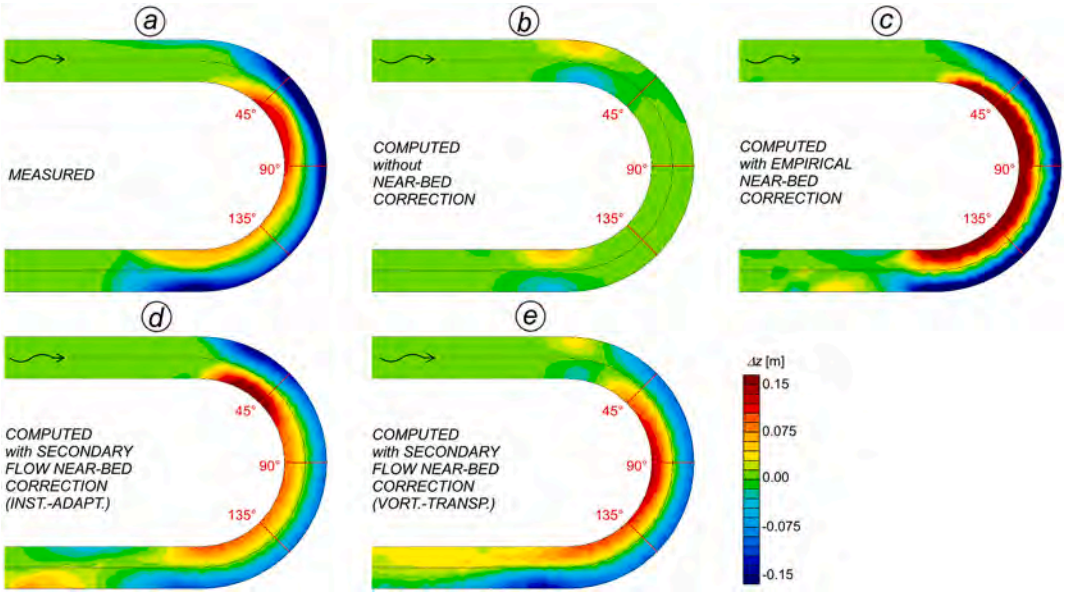

Fig. 16. Bed elevation with respect to the undisturbed flat bed ($\Delta z > 0$ denotes deposition, $\Delta z < 0$ erosion). a) Experimental data reproduced from Koch and Flokstra (1980); b) model results without any correction for bed-load direction; c) model results with empirical bed-load direction correction ($A = 10$ in Eq. (36)); d) model results with dispersive terms correction (instantaneous-adaptation approach), e) model results with dispersive terms correction (vorticity-transport approach).

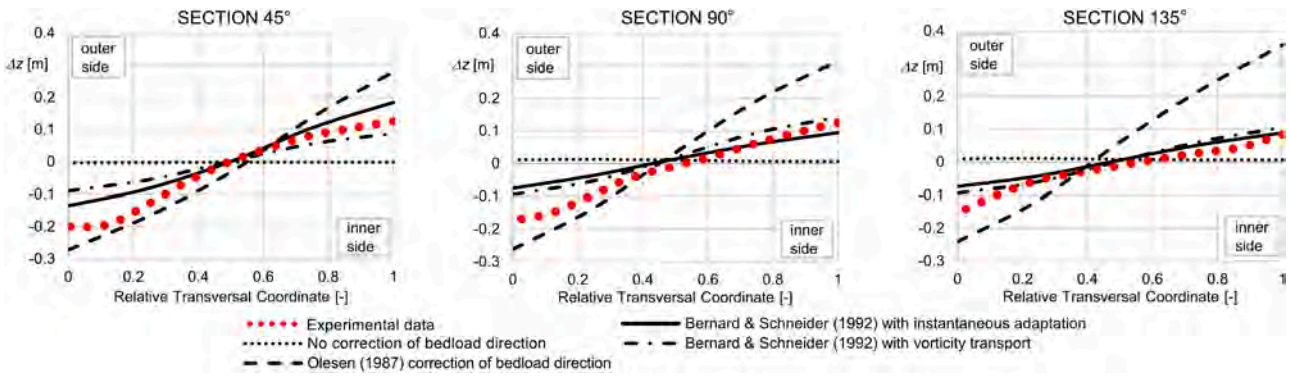

Fig. 17. Transversal profiles of bed elevation at 45°, 90°, and 135°with the results provided by different modelling approaches compared to the Koch and Flokstra (1980) experimental data.

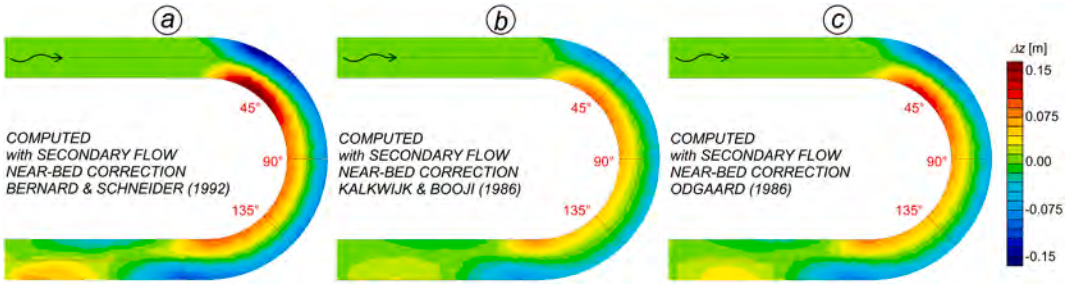

Fig. 18. Bed topography in terms of erosion/deposition with respect to a flat bed, computed with the dispersive terms corrections computed using the instantaneous-adaptation approach and the formulations of (a) Bernard and Schneider (1992), (b) Kalkwijk and Booji (1986), and (c) Odgaard (1986).

Fig. 19. The meandering reach of the Po River (Italy) between the Mincio and Panaro confluences.

$w = 2$ m/s isoline is plotted for both the cases with (magenta) and without (orange) the dispersive stresses, again without any substantial difference. These results suggest that including the dispersive terms for curvature-induced secondary flow is inessential to model the depth-averaged 2D flow field in natural rivers with fixed, deformed bed. Nonetheless, it has been already pointed out that secondary flow plays a major role with respect to the development of the bed topography (Blanckaert, 2010; Shimizu et al., 1990).

The Po River case study is then used to check the ability of the different approaches for curvature-induced secondary flow in modelling the relevant hydro-morphodynamic processes and to produce real-like bathymetric configurations. Hence, a set of mobile-bed simulations has been run starting from a flat bed, i.e., an unbalanced bathymetric configuration obtained by linearly interpolating the bed elevation from the mesh inlet to the outlet (Fig. 22b, the surveyed bed is shown in Fig. 22a). The movable-bed simulations, either with or without dispersive terms and correction for bedload direction, are run with a constant

Table 2
Po River case study. Characteristics of the simulations and relevant flow variables for scenarios Q_3990, Q_7400, and Q_11,500; the depth-average velocity is computed either neglecting (w) or considering (w^*) the dispersive terms.

		Q_3990			Q_7400			Q_11,500		
Discharge	[m^3/s]	3990			7400			11,500		
Downstream water ***level***	[m]	8			12			16		
		M1	**M2**	**M3**	**M1**	**M2**	**M3**	**M1**	**M2**	**M3**
Y_{MAX}	[m]	21.5	20.6	20.8	25.1	24.5	25.0	28.7	28.0	28.8
R	[m]	480	630	570	480	630	570	480	630	570
w_{MAX}	[m/s]	2.71	2.59	2.32	3.95	3.27	2.59	4.37	3.39	2.58
D_{s_MAX}	[Pa]	29	23	22	50	28	26	53	49	29
v_{s_MAX}	[m/s]	0.27	0.30	0.35	0.41	0.32	0.41	0.51	0.36	0.23
w^*_{MAX}	[m/s]	2.91	2.68	2.45	4.24	3.30	2.65	4.66	3.98	2.59
w^*_{MAX} / w_{MAX}	[-]	1.07	1.03	1.06	1.07	1.01	1.02	1.07	1.17	1.01

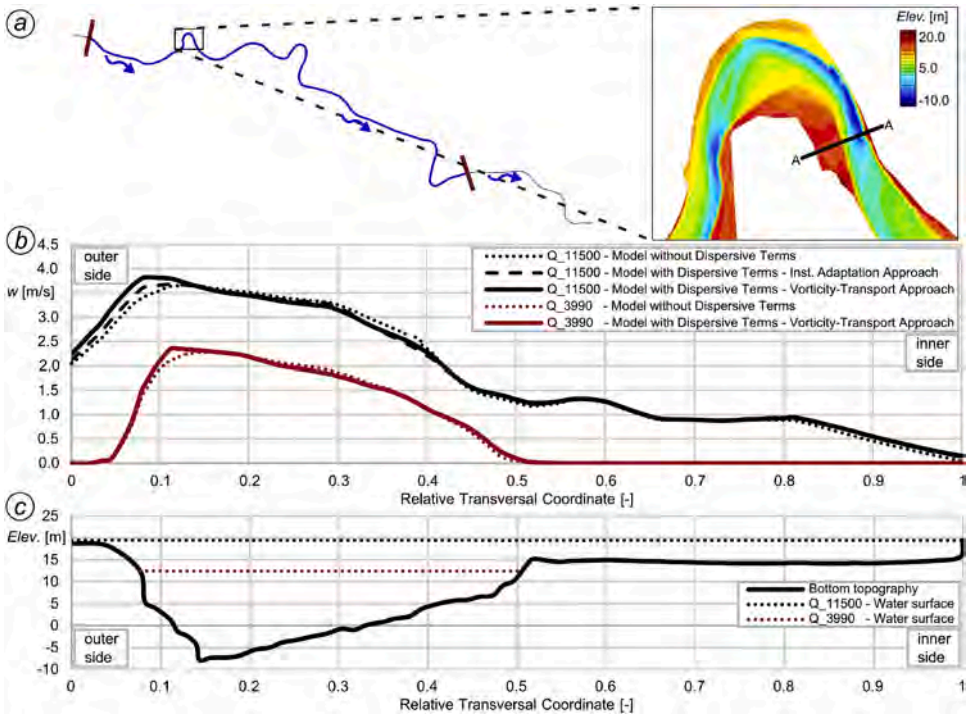

Fig. 20. Po River case study. Transversal profiles at the AA cross-section (at meander M1, panel a) of the depth-average velocity (b) and water and bed levels (c).

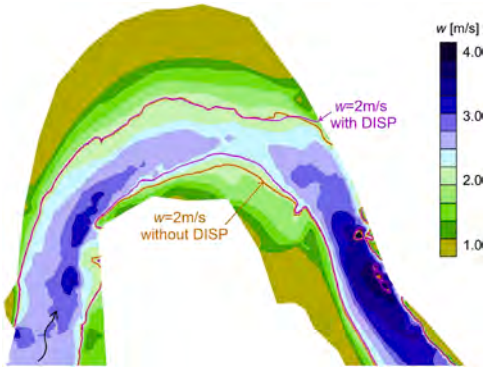

Fig. 21. Spatial distribution of the depth-average velocity at meander M1 for Q_11,500 and isoline for $w = 2$ m/s without (orange) and with (magenta) dispersive terms in the momentum equations.

discharge $Q = 11{,}500$ m^3/s until an equilibrium bed condition is reached. The inclusion of dispersive stresses and the correction for bedload direction are actually necessary to obtain reliable bed configurations, as demonstrated by comparing the equilibrium configuration obtained in the two different modelling approaches (Fig. 22c).

Interestingly, reliable equilibrium bathymetries are obtained also using the empirical correction for the bedload direction proposed by Olesen (1987), with $A_c = 10$, or considering a lower discharge of $Q = 7400$ m^3/s (see Figure S11 of the Supplementary Material).

Fig. 23 shows the bed evolution and the depth-averaged velocity field, from the initially flat bed to the equilibrium condition (reached at time $T_{eq} \approx 2$ years), modelled considering the dispersive terms. With the flat bed, the high-velocity thread is located at the inner part of the bend, and the flow then collides at an oblique angle with the outer bank; in this situation, the secondary flow is relatively strong, and so is the velocity redistribution entailed by the dispersive terms. As time advances, sediments are carried toward the accreting point bar, in the inner part of the bend, due to the inward direction imposed by the helical flow. The main part of the discharge then flows over the deepest part of the bend, driven by the so-called topographic steering (Blanckaert, 2010) more than by momentum redistribution induced by the secondary flow. Approaching the equilibrium condition, the importance of topographic steering increases, and the already weak effect of dispersive terms further reduces.

4. Discussion

This study deals with the inclusion of helical flow secondary currents in two-dimensional, general-purpose, river- and flood-models. The implementation of different modelling approaches and the application to several case studies, both in the laboratory and in the field, shed light on a set of interesting issues, which are here discussed.

4.1. The role of dispersive terms in momentum and transport-diffusion equations

The model applications described in the previous section highlighted the importance of including the dispersive terms; yet, not all these terms play an important role, nor are always necessary.

In the momentum equations, the most important contribution is given by the diagonal term D_{sn}; its spatial gradient entails additional resistance at the inner side of bends and acceleration at the outer side of bends (Dietrich and Smith, 1983), which are the outcome of the outward momentum transfer generated by the helical flow. The D_{ss} and D_{nn} terms are often neglected in the technical literature (e.g., Finnie et al., 1999). Indeed, the streamwise variation of D_{ss} is generally smooth, and the D_{nn} term is typically much smaller than D_{sn} when the curvature ratio, Y/R, is much lower than 1 (Lien et al., 1999). In the model applications described above, the inclusion of the D_{ss} and D_{nn} terms (not shown) produced negligible modifications in the model outcomes.

In the equation for transport and diffusion of conservative tracers and suspended matters, the inclusion of dispersive terms suffices to avoid the calibration of the Schmidt number to match experimental data. However, in transport/diffusion problems, the mesh resolution is the key factor to control the numerical diffusion and to obtain reliable results.

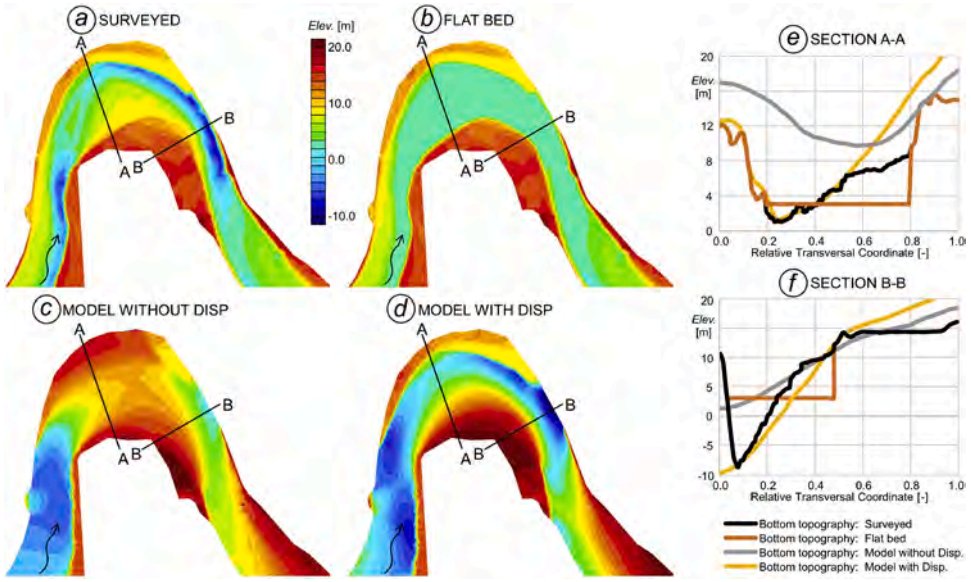

Fig. 22. Po River case study, meander bend M1. Surveyed bathymetry (a), flat bed used as initial condition for mobile-bed simulations (b), bed equilibrium condition modelled without (c) and with (d) dispersive terms and correction of bedload direction (vorticity-transport approach). The different bed configurations are also shown at cross-sections AA and BB (e,f).

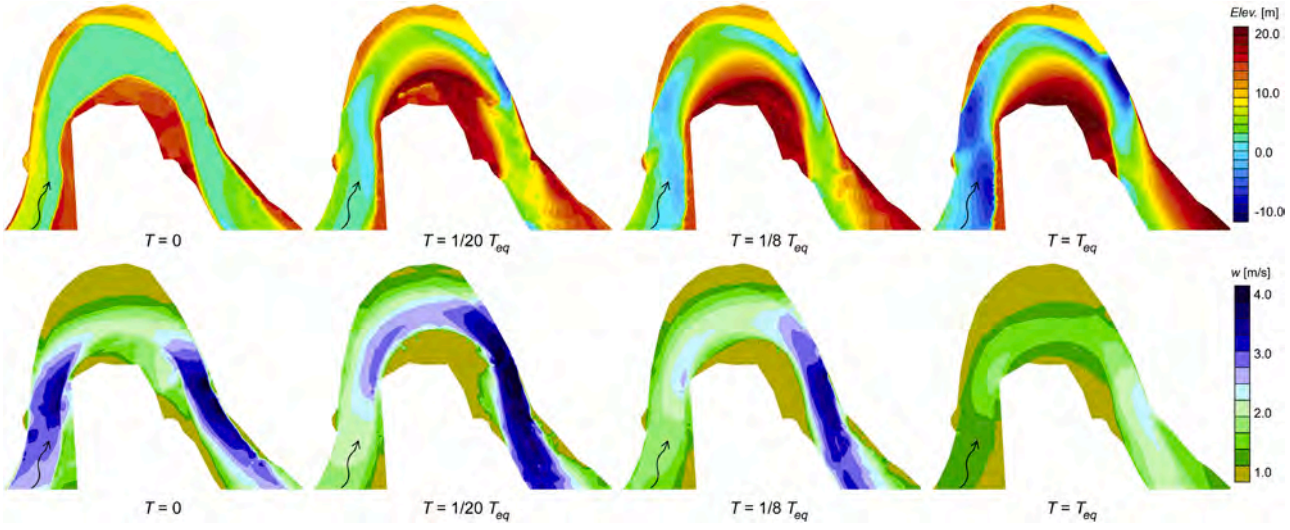

Fig. 23. Po River case study, meander bend M1. Bed evolution from an initial flat bed up to the equilibrium condition: modelled bathymetry (upper row) and flow velocity (lower row) at different time instants (0, 1/20 T_{eq}, 1/8 T_{eq}, and T_{eq}), with the time needed to reach the equilibrium condition being $T_{eq} \approx 2$ years.

4.2. Model sensitivity to the mesh resolution

The dispersive terms for curvature-induced secondary flows rely on the proper evaluation of the transversal gradient of the D_{sn} dispersive stress. The effectiveness of the helical-flow parameterization then depends on the mesh resolution. We performed an ad-hoc sensitivity analysis of the model results to the mesh resolution for the above case studies.

As a representative example, we considered the RIPRAP experiment and compared the model results obtained with four different mesh (Fig. 24):

- *mesh_1x*: cell-side-length $\approx$ 2.00 m, $B/\Delta x = 4$, tot. 1,112 cells;
- *mesh_10x*: cell-side-length $\approx$ 0.45 m, $B/\Delta x = 10$, tot. 11,528 cells;
- *mesh_40x*: cell-side-length $\approx$ 0.22 m, $B/\Delta x = 24$, tot. 43,395 cells;
- *mesh_160x*: cell-side-length $\approx$ 0.11 m, $B/\Delta x = 48$, tot. 166,965 cells;

with $B/\Delta x$ the channel width to cell-side-length ratio.

Fig. 24 shows that the dispersive terms, which come from the transversal derivatives of the D_{sn} stresses, are smoothed out excessively using the coarsest *mesh_1x*. The *mesh_10x* well adheres to the experimental velocity data (Fig. 24f). The *mesh_40x* improves the representation of dispersive terms, particularly close to the channel walls where the highest gradients of dispersive terms are located (Fig. 24b), leading to an improved spanwise distribution of flow velocity (Fig. 24f). Finally, as shown in Fig. 24g, the far increased computational need required by *mesh_160x* (vertical bars) is not counterbalanced by a further improvement of the solution (the velocity RMSE does not reduce for $B/\Delta x > 10$).

The mesh resolution was shown to have a far more important role in controlling the numerical diffusion of passive tracers and suspended matters (Sect. 3.3), which requires finer meshes ($B/\Delta x \approx 40$) than for including the parameterization of secondary-flow on momentum equations only ($B/\Delta x \approx 10 \div 20$). Using a coarser mesh with the Schmidt number tuned to larger values is a computationally efficient alternative;

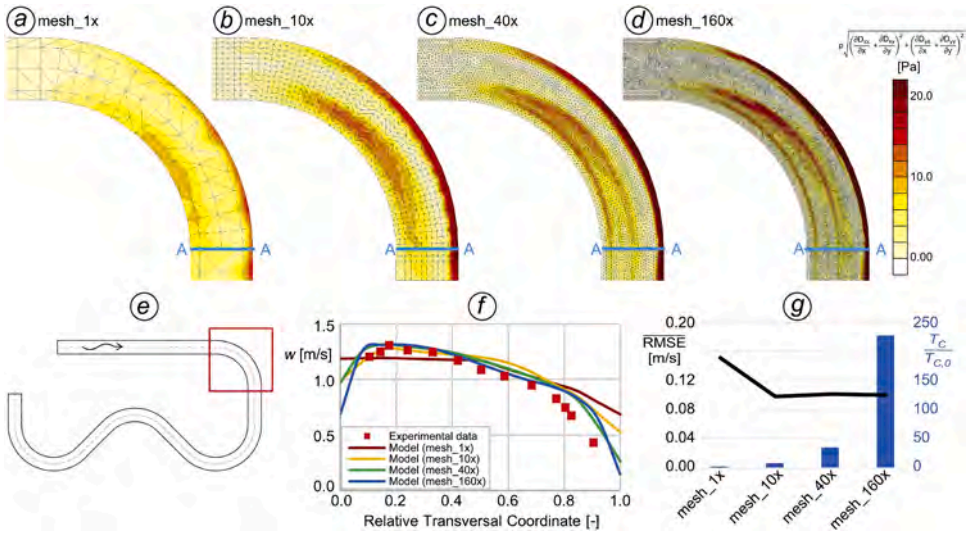

Fig. 24. (a-d) Magnitude of dispersive terms in the first bend of the RIPRAP facility channel for different mesh resolutions; (e) location of the first bend, and (f) transversal distribution of depth-averaged flow velocity at cross-section AA for the different mesh resolutions; (g) computational time (vertical bars) with respect to that of the 1x mesh, and velocity RMSE (black line) for the different mesh resolutions.

however, it entails extra diffusion in straight river segments and a loss of predictive ability (ad-hoc calibration becomes mandatory).

The choice of the grid structure (e.g., structured or unstructured, regular or irregular) is another issue that can affect the numerical diffusion of transported tracers (Casulli and Zanolli, 2005). While unstructured meshes allow for a greater flexibility and easier adaptation to irregular boundaries, the computation of the spatial gradients of dispersive stresses may become challenging close to geometrical singularities and at interfaces where the elements size changes abruptly (Nabi et al., 2016). An ad-hoc sensitivity analysis (not shown here) demonstrated that, when a proper mesh resolution is chosen, the schemes described at Sects. 2.6 leads to an accurate estimation of the spatial gradients irrespective of the kind of structured mesh employed (e.g., regular, aligned with flow, or irregular cell patterns).

4.3. Modelling approaches to dispersive stress estimation

Different options have been implemented to estimate the helical flow intensity, which regard the local or transported approach (i.e., with instantaneous adaptation or by transporting the streamwise vorticity component), the theoretical formulation for the secondary flow parameterization (i.e., the expression for k_P and k_D in Eqs. (10) or (11)), the inclusion of wall functions and of a non-linear model for secondary flow saturation. The choice of the most suitable approach mainly depends on the geometrical configuration of the channel. Here we collect some general criteria.

The local approach is the easiest to implement, the cheapest from a computational standpoint, and particularly suitable for long, regular bends. As it neglects the secondary-flow inertia, the helical flow intensity can be overpredicted in high-curvature bends, especially at the entrance of the bend, or mispredicted in tight succession of counter-rotating bends. Moreover, the local approach is very sensitive to geometrical singularities that entail abrupt variations of streamline curvature (also in straight river segments, where spurious local variations of dispersive stresses can appear). Thus, to avoid the onset of unphysical dispersive stresses, it is a good practice to apply a spatial smoothing (e.g., a Shapiro filter, Shapiro, 1970) to the streamline curvature field. The vorticity-transport approach, which intrinsically smooths out possible unevenness in the streamline curvature field as a result of the secondary flow inertia, is surely more robust and physically sound, yet more demanding from a computational standpoint. It is advisable for river channels in which the bathymetry presents some unevenness, in the case of sharp bends, and in tight sequences of bends.

The different parameterizations of secondary flow here implemented (see Table 1) lead to dispersive stresses, D_{ij}, whose magnitude are quite different; however, the dispersive terms in the momentum equations, which depend on the spatial gradients of D_{ij}, are coherently predicted by the different parameterizations. The model applications of Sect. 3 suggested that the different theoretical formulations are practically equivalent to each other.

The magnitude of dispersive terms in momentum equations, which depends on the gradients of dispersive stresses D_{ij}, is generally negligible at the channel centreline and maximum towards the banks, where both flow velocity and the dispersive stress tend to zero (Blanckaert, 2001; Johannesson and Parker, 1989a). In case of compact, low aspect-ratio cross-sections, the velocity gradient at the banks is greatly affected by the no-slip condition at the channel walls. In these cases, which are generally found in laboratory flumes, the use of wall functions to account for side-wall friction is mandatory. Instead, in natural bends, the effect of lateral wall is less significant as banks are tilted and the aspect ratio is far larger; in this kind of cross-sections, velocity reduces progressively in the transversal direction, dictated by the progressive reduction of water depth. Consequently, the free-slip condition at sidewalls is generally an acceptable hypothesis in natural rivers.

Finally, the model applications showed that the saturation of secondary flow has to be accounted for, to limit the intensity of helical flow, when strong secondary currents act to flatten the vertical profile of the streamwise velocity component (Blanckaert, 2009; Blanckaert et al., 2013). When (and where) the saturation effect becomes important is not only a function of the bend curvature, but also of the local flow field. Indeed, the key parameter governing the occurring of saturation is the spanwise gradient of the longitudinal velocity component, which describes if the high-velocity thread locates at the inner (free-vortex type flow) or at the outer (forced-vortex type flow) of the bend. Importantly, the local flow field and the transversal gradient of velocity, α_s, also depend on the bed bathymetry, i.e., flat or deformed (outward tilted).

This can be seen also by looking at the spatial distribution of the parameter α_s (the normalized transversal gradient of the depth-averaged velocity). For a flat-bed rectangular cross-section, α_s is expected to approach -1 at the beginning of the bend (free-vortex flow type) and to progressively increase along the bend to denote forced-vortex flow type (Blanckaert, 2010). This is roughly depicted by the plots in the second line of Fig. 7. Instead, in a real bend with deformed bed, the high-velocity thread locates at the outer side of the bend due to

topographic steering, keeping $\alpha_s \approx 1$ at the inner side, and $\alpha_s \approx -1$ at the outer side all along the bend (Figure S12 in the Supplementary Material). As a result, the helical flow intensity is dampened by the saturation model ($f_D << 1$) at the main core of the flow (outer side of the bend) where the velocity and the centrifugal force are highest, and limited by the low streamwise velocity at the inner side of the bend (where the dampening factor $f_D \approx 1$ would let the helical flow to develop free). Interestingly, when the depth-averaged flow field is mainly driven by the bathymetry, the spatial distribution of α_s remains broadly the same either considering or ignoring the dispersive terms (Figure S12 in the Supplementary Material). The role of bend bathymetry is further discussed in Sect. 4.5.

A relevant aspect concerning the model implementation is that the saturation effect can be effectively assessed with a pure 2D approach thus avoiding any reference to the channel centreline or width (Gu et al., 2016; Ottevanger et al., 2012), nor requiring time-consuming iterative procedures to estimate the non-linear parameters (Qin et al., 2019). In this way, the validity of traditional 2D models is extended to relatively sharp bends in a straightforward manner and without dramatic increase of the computational burden. The modeller should be aware that 2D models, equipped with this kind of description of secondary flows, cannot represent the formation of counterrotating secondary cells in very sharp bend (Blanckaert and de Vriend, 2010; Stoesser et al., 2010).

4.4. Ill-posedness and instability in 2D secondary flow models

The recent study by Chavarrías et al. (2019) highlighted an important issue concerning the possible ill-posedness of 2D depth-averaged models with linear formulation for the secondary flow. They considered the case in which the helical flow intensity is computed using a transport equation. Ill-posedness was shown to appear in the form of non-physical oscillations of the flow field, which increase with increased grid refinement. They demonstrated that adding a certain amount of diffusion, particularly in the spanwise direction, may lead to a well-posed problem and provide stable solutions. Besides that, they observed that accounting for the saturation effect may have a similar stabilizing effect, as saturation models act to dampen any kind of unbounded production of helical flow intensity, as in the case of unstable short waves.

On the one hand, we stress that, while 2D models compute the intensity of the helical flow locally, the secondary flow typically emerges as a unique rotating cell in the physical domain. Hence, to be physically consistent, the helical flow intensity computed by 2D models should vary smoothly in the spanwise direction. Of course, enhanced transversal diffusion, as that provided by the use of coarse grids, is beneficial in this regard. On the other hand, it is interesting to note that, in the numerical experiments by Chavarrías et al. (2019), model instabilities as a result of ill-posedness were significant for a grid with $B/\Delta x = 100$ and disappeared when they used a coarser grid with $B/\Delta x = 10$, comparable with the grid resolution used (and suggested as reasonable) in the present study.

4.5. The interplay of secondary flow and bed bathymetry

The importance of secondary flow in shaping hydro- and morphodynamics in curved channels, as well as the ability of 2D models to effectively capture the effects of helical flow, have been long debated in the literature (Alho and Mäkinen, 2010; Guan et al., 2016; Kasvi et al., 2015; 2013; Lane, 1998). A tangled picture also emerges from the case studies assessed in Sect. 3. Including the dispersive terms in the momentum equations was crucial in the case of laboratory experiments, yet it entailed minor changes to the flow field in the real-world case of the Po River considering the surveyed bed bathymetry. The different behaviour might be attributed to different curvature ratios among these tests. We then computed, for the model applications presented in Sect. 3, different scaling parameters that have been proposed to measure the strength of curvature-induced secondary flow and its effects on hydrodynamic (Kashyap et al., 2012). According to the values collected in Table 3, the secondary flow correction is most important in the EPFL channel of Blanckaert and de Vriend (2003), followed by that of Rozovskii (1957), and less important for the Chang (1971) case. This ranking agrees with the outcomes of the model applications shown in Sect. 3.1 and 3.3, respectively. In fact, we used the experimental data by Chang (1971) only to check the transport and diffusion module, because the effect of dispersive terms on the depth-averaged 2D hydrodynamics was negligible. Looking at the Po River case study, the parameters of Table 3 values are actually lower than most of their laboratory counterparts, but not sufficiently small to justify the weak to negligible effect of secondary flows on the depth-averaged hydrodynamics of the Po River test case. Similarly, the velocity redistribution by secondary flow is known to be much important for narrow cross-sections (e.g., $B/Y \approx 10$) and negligible in shallow ones with $B/Y > 50$ (Blanckaert, 2011; Blanckaert and de Vriend, 2010; Constantinescu et al., 2013) but, again, the aspect ratio of the Po River case study is not so different to justify the basically different behaviour.

The above considerations and the results shown in Sect. 3.5 suggest that the main reason for the controversial results obtained in the previous and present applications stems from the fact that the development of (and the role played by) secondary flows essentially depends on the bed bathymetry. In the Po River test, the surveyed bottom is deformed (see the cross-section in Fig. 20 and the colour map in Fig. 22a), whereas the laboratory tests dealt with compact cross-sections with flat bed and vertical walls. By performing additional numerical experiments in which the bed was artificially flattened, it was shown that the flow field in the Po River bends is mainly driven by the bed topography (i.e., the so-called topographic steering) than by momentum exchanges and velocity redistribution ascribed to curvature-induced secondary flow (Blanckaert, 2010; Chen and Duan, 2006; Deng et al., 2021; He, 2018; van Balen et al., 2010).

Of course, the fact that the depth-averaged 2D flow field is not significantly altered by the secondary circulation and can be roughly predicted by traditional 2D models without including dispersive terms, does not imply that secondary circulations do no play a role at all. Secondary circulations, causing the inner and outer streamwise-oriented vortical cells, still amplify the boundary shear stresses, altering the transport of sediments and posing a threat to bank stability; this picture further complicates in very sharp bends (Blanckaert, 2011; Constantinescu et al., 2013). Accounting for the effects of curvature-induced secondary flow in 2D hydro-morphological models remains almost necessary, in particular when the bathymetric configuration is far from equilibrium conditions (Shimizu et al., 1990), or when the bathymetry could be subject to strong variations (e.g., long-term simulations). However, the vast majority of natural river bends are mildly curved and/or have a deformed bed; in these conditions, the depth-averaged 2D flow field is nearly independent of dispersive terms, and the major outcome of curvature-induced secondary circulations is by far the change in bedload direction. This explains why many hydro-morphological models, to account for the effect of secondary flows, only implement empirical formulations to correct the bedload direction (e.g., Defina, 2003; Vanzo et al., 2021).

5. Conclusions

A correction for curvature-induced secondary flow in channel and river bends is implemented in the hydro- and morpho-dynamic model 2DEF. The dispersive terms appearing in the momentum equations are expressed according to three different formulations, recast in similar form. The computation can be performed assuming the instantaneous-adaptation of secondary flow to the driving streamline curvature, or accounting for inertia and phase-lag of the helical flow via a vorticity-transport approach. The effect of impervious banks is accounted for using wall functions. The classical linear model for secondary flow is

Table 3
Scaling parameters for the strength of curvature-induced secondary flow computed for the case studies presented in Sect. 3.

Case study	Trial	Effects on flow field		Scaling parameter for secondary flow strength					
				Odgaard (1989)	Johannesson & Parker (1989b)	Bolla Pittaluga et al. (2009)	Blanckaert and de Vriend (2003)	Blanckaert and de Vriend (2010)	
			$\frac{B}{Y}$	$\frac{Y}{R}\times\ 100$	$C_f^{-1}\frac{2Y}{B}$	$C_f^{-1/2}\frac{Y}{R}$	$C_f^{-0.275}\left(\frac{Y}{R}\right)^{0.5}$	$C_f^{-1}\frac{Y}{R}$	$\frac{B}{R}$
Chang (1971)	–	no	19.17	1.41	4.11	0.09	0.33	0.56	0.27
RIPRAP facility	–	yes	6.50	5.33	43.16	0.63	0.90	7.48	0.35
LFM flume	–	yes	8.50	5.00	89.77	0.98	1.15	19.08	0.43
EPFL channel	Q_104	yes	6.10	12.53	71.82	1.85	1.56	27.46	0.76
EPFL channel	Q_89	yes	8.13	9.41	49.04	1.33	1.32	18.75	0.76
EPFL channel	Q_56	yes	11.93	6.41	29.40	0.85	1.05	11.24	0.76
Rozovskii	–	yes	13.33	7.50	29.33	1.05	1.17	14.67	1.00
Po River case study	Q_11,500	weak	12.50	3.33	65.76	0.68	0.96	13.70	0.42
	Q_7400	no	16.67	2.50	44.81	0.48	0.81	9.34	0.42
	Q_3990	no	25	1.67	27.42	0.31	0.64	5.71	0.42

completed with a novel, pure 2D implementation of a robust non-linear model accounting for the saturation of secondary flow occurring in relatively sharp bends. Dispersive terms are added also to the transport and diffusion equation, and accounted for in the morphodynamic module for bedload transport and mobile bed evolution.

Model applications to laboratory tests and to a real river, with both fixed and mobile beds, confirm the importance of accounting for secondary flow and the validity of the approaches. The different formulations for dispersive terms perform similarly to each other. The local, instantaneous-adaptation approach is less demanding and suitable to isolated bends in riverbeds with a regular bathymetry (the streamline curvature field must be smoothed out to avoid numerical instabilities). All the local approaches (either to compute the dispersive stresses or to correct the direction of bedload transport) produce unphysical results in presence of geometrical singularities such as bridge piers or abutments. The inertia of secondary flow, which is accounted for intrinsically when transporting the streamwise vorticity, filters out the typical unevenness characterizing the bathymetry and the curvature field of real rivers and possible geometrical singularities.

The non-linear model for secondary flow saturation is a fundamental ingredient to counteract the excessive growth of helical flow intensity in relatively sharp bends and to produce physically sound spatial distributions of dispersive stresses. To this purpose, wall functions are needed to model the effect of vertical, impervious walls; nonetheless, in real rivers with tilted banks, wall functions are unnecessary.

Curvature-induced secondary flows are shown to produce important modifications to the depth-averaged flow field in case of rectangular cross-sections (i.e., flat bed in the spanwise direction). The high-velocity thread is moved from the inner to the outer side of the bend, and saturation of secondary flow soon becomes important, even for not excessively sharp bends. On the contrary, in real rivers with formed bathymetry (outer scour) the moderate streamline curvature and the already-formed bed bathymetry make the effects of the correction less evident in terms of depth-averaged flow field. The estimation of secondary flow intensity remains important for modelling the transport of suspended matter and, above all, for repercussions on bedload transport and morphological setting. However, in real river with formed bathymetry, empirical corrections for the direction of bedload transport, based on the local streamline curvature and without including dispersive terms in the momentum equations, generally perform satisfactorily.

Funding

T.L. is sponsored by a PhD scholarship funded by the *CARIPARO* Foundation. D.P.V. has been partly supported by the Italian National Research Programme PRIN 2017, with the project n. 2017SEB7Z8 "*IntEractions between hydrodyNamics flows and bioTic communities in fluvial Ecosystems: advancement in dischaRge monitoring and understanding of Processes Relevant for ecosystem sustaInability by the development of novel technologies with fIeld observatioNs and laboratory testinG (ENTERPRISING)*"

CRediT authorship contribution statement

Tommaso Lazzarin: Conceptualization, Methodology, Validation, Investigation, Visualization, Writing – original draft. **Daniele P. Viero:** Conceptualization, Methodology, Supervision, Writing – review & editing.

Declaration of Competing Interest

The authors declare that they have no known competing financial interests or personal relationships that could have appeared to influence the work reported in this paper.

Data availability

Data will be made available on request.

Acknowledgments

Prof. Andrea Defina is gratefully acknowledged for fruitful discussions.

Supplementary materials

Supplementary material associated with this article can be found, in the online version, at doi:10.1016/j.advwatres.2022.104355.

References

Abad, J.D., Buscaglia, G.C., Garcia, M.H., 2008. 2D stream hydrodynamic, sediment transport and bed morphology model for engineering applications. Hydrol. Process 22, 1443–1459. https://doi.org/10.1002/hyp.6697.

Abad, J.D., Garcia, M.H., 2009. Experiments in a high-amplitude Kinoshita meandering channel: 1. Implications of bend orientation on mean and turbulent flow structure. Water Resour. Res. 45 https://doi.org/10.1029/2008WR007016. W02401.

Ahmadi, M., Ayyoubzadeh, S., Montazeri Namin, M., Samani, J., 2009. A 2D numerical depth-averaged model for unsteady flow in open channel bends. J. Agric. Sci. 11, 457–468.

Alavian, V., 1986. Dispersion tensor in rotating flows. J. Hydraul. Eng. 112, 771–777. https://doi.org/10.1061/(ASCE)0733-9429(1986)112:8(771).

Alho, P., Mäkinen, J., 2010. Hydraulic parameter estimations of a 2D model validated with sedimentological findings in the point bar environment. Hydrol. Process. 24, 2578–2593. https://doi.org/10.1002/hyp.7671.

Baar, A.W., de Smit, J., Uijttewaal, W.S.J., Kleinhans, M.G., 2018. Sediment transport of fine sand to fine gravel on transverse bed slopes in rotating annular flume experiments. Water Resour. Res. 54, 19–45. https://doi.org/10.1002/2017WR020604.

Bai, R., Zhu, D., Chen, H., Li, D., 2019. Laboratory study of secondary flow in an open channel bend by using PIV. Water 11, 659. https://doi.org/10.3390/w11040659.

Bates, P.D., 2022. Flood inundation prediction. Annu. Rev. Fluid Mech. 54, 287–315. https://doi.org/10.1146/annurev-fluid-030121-113138.

Bathurst, J.C., Thorne, C.R., Hey, R.D., 1977. Direct measurements of secondary currents in river bends. Nature 269, 504–506. https://doi.org/10.1038/269504a0.

Begnudelli, L., Valiani, A., Sanders, B.F., 2010. A balanced treatment of secondary currents, turbulence and dispersion in a depth-integrated hydrodynamic and bed deformation model for channel bends. Adv. Water Resour. 33, 17–33. https://doi.org/10.1016/j.advwatres.2009.10.004.

Bernard, R.S., Schneider, M., 1992. Depth-Averaged Numerical Modeling For Curved Channels. Tech. Rep. HL-92-9. U.S. Army Engineer Waterways Experiment Station, Vicksburg, Miss.

Blanckaert, K., 2011. Hydrodynamic processes in sharp meander bends and their morphological implications. J. Geophys. Res. 116, F01003. https://doi.org/10.1029/2010JF001806.

Blanckaert, K., 2010. Topographic steering, flow recirculation, velocity redistribution, and bed topography in sharp meander bends. Water Resour. Res. 46, W09506. https://doi.org/10.1029/2009WR008303.

Blanckaert, K., 2009. Saturation of curvature-induced secondary flow, energy losses, and turbulence in sharp open-channel bends: laboratory experiments, analysis, and modeling. J. Geophys. Res. 114, F03015. https://doi.org/10.1029/2008JF001137.

Blanckaert, K., 2001. Discussion of "Bend-flow simulation using 2D depth-averaged model.". J. Hydraul. Eng. 127, 167–170. https://doi.org/10.1061/(ASCE)0733-9429(2001)127:2(167).

Blanckaert, K., Constantinescu, G., Uijttewaal, W., Chen, Q., 2013. Hydro- and morphodynamics in curved river reaches; recent results and directions for future research. Adv. Geosci. 37, 19–25. https://doi.org/10.5194/adgeo-37-19-2013.

Blanckaert, K., de Vriend, H., 2004. Secondary flow in sharp open-channel bends. J. Fluid Mech. 498, 353–380. https://doi.org/10.1017/S0022112003006979.

Blanckaert, K., de Vriend, H.J., 2010. Meander dynamics: a nonlinear model without curvature restrictions for flow in open-channel bends. J. Geophys. Res. 115, F0401. https://doi.org/10.1029/2009JF001301.

Blanckaert, K., de Vriend, H.J., 2003. Nonlinear modeling of mean flow redistribution in curved open channels. Water Resour. Res. 39, 1375. https://doi.org/10.1029/2003WR002068.

Blanckaert, K., Graf, W.H., 2004. Momentum transport in sharp open-channel bends. J. Hydraul. Eng. 130, 186–198. https://doi.org/10.1061/(ASCE)0733-9429(2004)130:3(186).

Bolla Pittaluga, M., Nobile, G., Seminara, G., 2009. A nonlinear model for river meandering. Water Resour. Res. 45, W04432. https://doi.org/10.1029/2008WR007298.

Bonetto, I., Defina, A., 1998. Rappresentazione dei termini di accelerazione convettiva in un modello bidimensionale della propagazione di onde lunghe in acque basse (Numerical discretization of the advective terms in a Finite Element shallow water equations model). In: Proc. of XVI Convegno di Idraulica e Costruzioni Idrauliche, pp. 53–64.

Bora, K., Khalita, H.M., 2020. A semi-coupled model for morphological flow simulation in river bend. J. Appl. Fluid Mech. 13, 1611–1622. https://doi.org/10.36884/jafm.13.05.30842.

Boussinesq, J., 1868. Mémoire sur l'influence des frottements dans les mouvements réguliers des fluides; XII- Essai sur Ie movement permanent d'un liquide dans un canal horizontal axe circulaire. J. Math Pures Appl. 413, 2eme Serie, Tome XIII.

Bowker, K., 1988. Albert Einstein and Meandering Rivers. Earth Sci. Hist. 7, 45. https://doi.org/10.17704/eshi.7.1.yk72n55q84qxu5n6.

Camporeale, C., Cannamela, F., Canuto, C., Manes, C., 2021. Stability analysis of open-channel flows with secondary currents. J. Fluid Mech. 927, A32. https://doi.org/10.1017/jfm.2021.769.

Camporeale, C., Perona, P., Porporato, A., Ridolfi, L., 2007. Hierarchy of models for meandering rivers and related morphodynamic processes. Rev. Geophys. 45, RG1001. https://doi.org/10.1029/2005RG000185.

Carniello, L., Defina, A., D'Alpaos, L., 2012. Modeling sand-mud transport induced by tidal currents and wind waves in shallow microtidal basins: application to the Venice Lagoon (Italy). Estuar. Coast. Shelf Sci. 102–103, 105–115. https://doi.org/10.1016/j.ecss.2012.03.016.

Casulli, V., Zanolli, P., 2005. High resolution methods for multidimensional advection–diffusion problems in free-surface hydrodynamics. Ocean Modell. 10, 137–151. https://doi.org/10.1016/j.ocemod.2004.06.007.

Cea, L., Bladé, E., 2015. A simple and efficient unstructured finite volume scheme for solving the shallow water equations in overland flow applications. Water Resour. Res. 51, 5464–5486. https://doi.org/10.1002/2014WR016547.

Chang, Y.C., 1971. Lateral Mixing in Meandering Channels. University of Iowa.

Chavarrías, V., Schielen, R., Ottevanger, W., Blom, A., 2019. Ill posedness in modelling two-dimensional morphodynamic problems: effects of bed slope and secondary flow. J. Fluid Mech. 868, 461–500. https://doi.org/10.1017/jfm.2019.166.

Chen, D., Duan, J.D., 2006. Simulating sine-generated meandering channel evolution with an analytical model. J. Hydraul. Res. 44, 363–373. https://doi.org/10.1080/00221686.2006.9521688.

Constantinescu, G., Kashyap, S., Tokyay, T., Rennie, C.D., Townsend, R.D., 2013. Hydrodynamic processes and sediment erosion mechanisms in an open channel bend of strong curvature with deformed bathymetry. J. Geophys. Res. 118, 480–496. https://doi.org/10.1002/jgrf.20042.

Crosato, A., Struiksma, N., 1989. Analysis of a 2 D Bed Topography Model For Rivers, in: River Meandering (Eds S. Ikeda and G. Parker), 153–180. https://doi.org/10.1029/WM012p0153.

D'Alpaos, L., Defina, A., 2007. Mathematical modeling of tidal hydrodynamics in shallow lagoons: a review of open issues and applications to the Venice lagoon. Comput. Geosci. 33, 476–496. https://doi.org/10.1016/j.cageo.2006.07.009.

De Vriend, H.J., 1981. Steady Flow in Shallow Channel Bends. Tech. Rep. 81-3. Fluid Mech. Lab., Dep. of Civ. Eng., Delft Univ. of Technol., Delft, Netherlands.

De Vriend, H.J., 1977. A mathematical model of steady flow in curved shallow channels. J. Hydraul. Res. 15, 37–54. https://doi.org/10.1080/00221687709499748.

Defina, A., 2003. Numerical experiments on bar growth. Water Resour. Res. 39, 1092. https://doi.org/10.1029/2002WR001455.

Defina, A., 2000. Two-dimensional shallow flow equations for partially dry areas. Water Resour. Res. 36, 3251–3264. https://doi.org/10.1029/2000WR900167.

Demuren, A.O., 1993. A numerical model for flow in meandering channels with natural bed topography. Water Resour. Res. 29, 1269–1277. https://doi.org/10.1029/92WR02907.

Demuren, A.O., Rodi, W., 1986. Calculation of flow and pollutant dispersion in meandering channels. J. Fluid Mech. 172, 63–92. https://doi.org/10.1017/S0022112086001659.

Deng, S., Xia, J., Zhou, M., Li, Z., Duan, G., Shen, J., Blanckaert, K., 2021. Secondary flow and flow redistribution in two sharp bends on the middle Yangtze River. Water Resour. Res. 57, e2020WR028534 https://doi.org/10.1029/2020WR028534.

Dietrich, W.E., Smith, J.D., 1983. Influence of the point bar on flow through curved channels. Water Resour. Res. 19, 1173–1192. https://doi.org/10.1029/WR019i005p01173.

Duan, J.G., 2004. Simulation of flow and mass dispersion in meandering channels. J. Hydraul. Eng. 130, 964–976. https://doi.org/10.1061/(ASCE)0733-9429(2004)130:10(964).

Duan, J.G., Nanda, S.K., 2006. Two-dimensional depth-averaged model simulation of suspended sediment concentration distribution in a groyne field. J Hydrol (Amst) 327, 426–437. https://doi.org/10.1016/j.jhydrol.2005.11.055.

Einstein, A., 1926. Die Ursache der Mäanderbildung der Flußläufe und des sogenannten Baerschen Gesetzes. Naturwissenschaften 14, 223–224. https://doi.org/10.1007/BF01510300.

Einstein, H.A., Li, H., 1958. Secondary currents in straight channels. Eos Trans. Am. Geophys. Union 39, 1085–1088. https://doi.org/10.1029/TR039i006p01085.

Elder, J.W., 1959. The dispersion of marked fluid in turbulent shear flow. J. Fluid Mech. 5, 544–560. https://doi.org/10.1017/S0022112059000374.

Engel, F.L., Rhoads, B.L., 2012. Interaction among mean flow, turbulence, bed morphology, bank failures and channel planform in an evolving compound meander loop. Geomorphology 163–164, 70–83. https://doi.org/10.1016/j.geomorph.2011.05.026.

Engmann, E., 1986. Effect of channel bends on transverse mixing. Nigerian J. Technol. 10, 57–72.

Falcon, M., 1984. Secondary flow in curved open channels. Annu Rev Fluid Mech 16, 179–193. https://doi.org/10.1146/annurev.fl.16.010184.001143.

Farhadi, A., Sindelar, C., Tritthart, M., Glas, M., Blanckaert, K., Habersack, H., 2018. An investigation on the outer bank cell of secondary flow in channel bends. J. Hydroenviron. Res. 18, 1–11. https://doi.org/10.1016/j.jher.2017.10.004.

Finnie, J., Donnell, B., Letter, J., Bernard, R.S., 1999. Secondary flow correction for depth-averaged flow calculations. J. Eng. Mech. 125, 848–863. https://doi.org/10.1061/(ASCE)0733-9399(1999)125:7(848).

Fischer, H.B., 1969. The effect of bends on dispersion in streams. Water Resour. Res. 5, 496–506. https://doi.org/10.1029/WR005i002p00496.

Fischer, H.B., List, J.E., Koh, C.R., Imberger, J., Brooks, N.H., 1979. Mixing in Inland and Coastal Waters. Academic Press, San Diego, California. https://doi.org/10.1016/C2009-0-22051-4.

Fischer-Antze, T., Olsen, N.R.B., Gutknecht, D., 2008. Three-dimensional CFD modeling of morphological bed changes in the Danube River. Water Resour. Res. 44, W09422. https://doi.org/10.1029/2007WR006402.

Ghamry, H.K., Steffler, P.M., 2002. Effect of applying different distribution shapes for velocities and pressure on simulation of curved open channels. J. Hydraul. Eng. 128, 969–982. https://doi.org/10.1061/(ASCE)0733-9429(2002)128:11(969).

Gu, L., Zhang, S., He, L., Chen, D., Blanckaert, K., Ottevanger, W., Zhang, Y., 2016. Modeling flow pattern and evolution of meandering channels with a nonlinear model. Water 8, 418. https://doi.org/10.3390/w8100418.

Guan, M., Wright, N.G., Sleigh, P.A., Ahilan, S., Lamb, R., 2016. Physical complexity to model morphological changes at a natural channel bend. Water Resour. Res. 52, 6348–6364. https://doi.org/10.1002/2015WR017917.

He, L., 2018. Distribution of primary and secondary currents in sine-generated bends. Water 44, 118. https://doi.org/10.4314/wsa.v44i1.14.

Holly, F.M., Usseglio-Polatera, J., 1984. Dispersion simulation in two-dimensional tidal flow. J. Hydraul. Eng. 110, 905–926. https://doi.org/10.1061/(ASCE)0733-9429(1984)110:7(905).

Horna-Munoz, D., Constantinescu, G., 2018. A fully 3-D numerical model to predict flood wave propagation and assess efficiency of flood protection measures. Adv. Water Resour. 122, 148–165. https://doi.org/10.1016/j.advwatres.2018.10.014.

Hu, D., Zhu, Y., Zhong, D., Qin, H., 2017. Two-dimensional finite-volume eulerian-lagrangian method on unstructured grid for solving advective transport of passive scalars in free-surface flows. J. Hydraul. Eng. 143, 04017051 https://doi.org/10.1061/(ASCE)HY.1943-7900.0001371.

Ikeda, S., Nishimura, T., 1986. Flow and Bed profile in meandering sand-silt rivers. J. Hydraul. Eng. 112, 562–579. https://doi.org/10.1061/(ASCE)0733-9429(1986)112:7(562).

Ikeda, S., Yamasaka, M., Kennedy, J.F., 1990. Three-dimensional fully developed shallow-water flow in mildly curved bends. Fluid Dyn. Res. 6, 155–173. https://doi.org/10.1016/0169-5983(90)90059-8.
Iwasaki, T., Shimizu, Y., Kimura, I., 2016. Sensitivity of free bar morphology in rivers to secondary flow modeling: linear stability analysis and numerical simulation. Adv. Water Resour. 92, 57–72. https://doi.org/10.1016/j.advwatres.2016.03.011.
Jang, C.-.L., Shimizu, Y., 2005. Numerical simulation of relatively wide, shallow channels with erodible banks. J. Hydraul. Eng. 131, 565–575. https://doi.org/10.1061/(ASCE)0733-9429(2005)131:7(565).
Jin, Y., Steffler, P.M., 1993. Predicting flow in curved open channels by depth-averaged method. J. Hydraul. Eng. 119, 109–124. https://doi.org/10.1061/(ASCE)0733-9429(1993)119:1(109).
Johannesson, H., Parker, G., 1989a. Velocity redistribution in meandering rivers. J. Hydraul. Eng. 115, 1019–1039. https://doi.org/10.1061/(ASCE)0733-9429(1989)115:8(1019).
Johannesson, H., Parker, G., 1989b. Secondary flow in mildly sinuous channel. J. Hydraul. Eng. 115, 289–308. https://doi.org/10.1061/(ASCE)0733-9429(1989)115:3(289).
Kalkwijk, J.P.Th., Booij, R., 1986. Adaptation of secondary flow in nearly-horizontal flow. J. Hydraul. Res. 24, 19–37. https://doi.org/10.1080/00221688609499330.
Kashyap, S., Constantinescu, G., Rennie, C.D., Post, G., Townsend, R., 2012. Influence of channel aspect ratio and curvature on flow, secondary circulation, and bed shear stress in a rectangular channel bend. J. Hydraul. Eng. 138, 1045–1059. https://doi.org/10.1061/(ASCE)HY.1943-7900.0000643.
Kasvi, E., Alho, P., Lotsari, E., Wang, Y., Kukko, A., Hyyppä, H., Hyyppä, J., 2015. Two-dimensional and three-dimensional computational models in hydrodynamic and morphodynamic reconstructions of a river bend: sensitivity and functionality. Hydrol. Process. 29, 1604–1629. https://doi.org/10.1002/hyp.10277.
Kasvi, E., Petteri, A., Vaaja, M., Hyyppä, H., Hyyppä, J., 2013. Spatial and temporal distribution of fluvio-morphological processes on a meander point bar during a flood event. Hydrol. Res. 44, 1022–1039. https://doi.org/10.2166/nh.2013.091.
Keylock, C.J., Constantinescu, G., Hardy, R.J., 2012. The application of computational fluid dynamics to natural river channels: eddy resolving versus mean flow approaches. Geomorphology 179, 1–20. https://doi.org/10.1016/j.geomorph.2012.09.006.
Kikkawa, H., Kitagawa, A., Ikeda, S., 1976. Flow and bed topography in curved open channels. J. Hydraul. Div. Am. Soc. Civ. Eng. 102, 1327–1342. https://doi.org/10.1061/JYCEAJ.0004615.
Kitanidis, P.K., Kennedy, J.F., 1984. Secondary current and river-meander formation. J. Fluid Mech. 144, 217–229. https://doi.org/10.1017/S0022112084001580.
Koch, F.G., Flokstra, C., 1980. Bed level computations for curved alluvial channels. In: Proc. of the XIX Congress of the IAHR, 2, pp. 357–364.
Koken, M., Constantinescu, G., Blanckaert, K., 2013. Hydrodynamic processes, sediment erosion mechanisms, and Reynolds-number-induced scale effects in an open channel bend of strong curvature with flat bathymetry. J. Geophys. Res. 118, 2308–2324. https://doi.org/10.1002/2013JF002760.
Lai, Y., Thomas, R., Ozeren, Y., Simon, A., Greimann, B., Wu, K., 2012. Coupling a two-dimensional model with a deterministic bank stability model. In: World Environmental and Water Resources Congress 2012: Crossing Boundaries, Proc. of the 2012 Congress, pp. 1290–1300. https://doi.org/10.1061/9780784412312.130.
Lane, S.N., 1998. Hydraulic modelling in hydrology and geomorphology: a review of high resolution approaches. Hydrol Process 12, 1131–1150. https://doi.org/10.1002/(SICI)1099-1085(19980630)12. :8<1131::AID−HYP611>3.0.CO;2-K.
Lee, M.E., Kim, G., 2012. Influence of secondary currents on solute dispersion in curved open channels. J. Appl. Math. 2012, 781695 https://doi.org/10.1155/2012/781695.
Lee, M.E., Seo, I.W., 2013. Spatially variable dispersion coefficients in meandering channels. J. Hydraul. Eng. 139, 141–153. https://doi.org/10.1061/(ASCE)HY.1943-7900.0000669.
Leschziner, M.A., Rodi, W., 1979. Calculation of strongly curved open channel flow. J. Hydraul. Div., Am. Soc. Civ. Eng. 105, 1297–1314. https://doi.org/10.1061/JYCEAJ.0005286.
Lien, H.C., Hsieh, T.Y., Yang, J.C., Yeh, K.C., 1999. Bend-flow simulation using 2D depth-averaged model. J. Hydraul. Eng. 125, 1097–1108. https://doi.org/10.1061/(ASCE)0733-9429(1999)125:10(1097).
Lou, S., Liu, H., Liu, S., Chen, M., Zhong, G., 2020. Longitudinal and lateral diffusion of solute transport in flow with rigid vegetation. Environ. Sci. Europe 32, 40. https://doi.org/10.1186/s12302-020-00315-8.
Moncho-Esteve, I.J., Folke, F., García-Villalba, M., Palau-Salvador, G., 2017. Influence of the secondary motions on pollutant mixing in a meandering open channel flow. Environ. Fluid Mech. 17, 695–714. https://doi.org/10.1007/s10652-017-9513-4.
Nabi, M., Ottevanger, W., Giri, S., 2016. Computational modelling of secondary flow on unstructured grids. In: River Sedimentation – Proc. of the 13th International Symposium on River Sedimentation, ISRS 2016. Stuttgart, Germany. London, pp. 719–726.
Nezu, I., 2005. Open-channel flow turbulence and its research prospect in the 21st century. J. Hydraul. Eng. 131, 229–246. https://doi.org/10.1061/(ASCE)0733-9429(2005)131:4(229).
Nikora, V., Roy, A.G., 2011. Secondary flows in rivers: theoretical framework, recent advances, and current challenges. Gravel-Bed Rivers. John Wiley & Sons, Ltd, pp. 1–22. https://doi.org/10.1002/9781119952497.ch1.
Odgaard, A.J., 1989. River Meander Model-I: development. J. Hydraul. Eng. 115, 1433–1450. https://doi.org/10.1061/(ASCE)0733-9429(1989)115:11(1433).
Odgaard, A.J., 1986. Meander Flow Model. I: development. J. Hydraul. Eng. 112, 1117–1135. https://doi.org/10.1061/(ASCE)0733-9429(1986)112:12(1117).
Olesen, K.W., 1987. Bed Topography in Shallow River Bends. Delft University of Technology.
Ottevanger, W., 2013. Modelling and Parametrizing the hydro- and morphodynamics of Curved Open Channels. Delft University of Technology.
Ottevanger, W., Blanckaert, K., Uijttewaal, W.S.J., 2012. Processes governing the flow redistribution in sharp river bends. Geomorphology 163–164, 45–55. https://doi.org/10.1016/j.geomorph.2011.04.049.
Papanicolaou, A.N., Elhakeem, M., Hilldale, R., 2007. Secondary current effects on cohesive river bank erosion. Water Resour. Res. 43, W12418. https://doi.org/10.1029/2006WR005763.
Pratap, V.S., Spalding, D.B., 1975. Numerical computations of the flow in curved ducts. Aeronaut. Quart. 26, 219–228. https://doi.org/10.1017/S0001925900007368.
Qin, C., Shao, X., Xiao, Y., 2019. Secondary flow effects on deposition of cohesive sediment in a meandering reach of Yangtze River. Water 11, 1444. https://doi.org/10.3390/w11071444.
Rishnappan, B.G.K., Lau, Y.L., 1977. Transverse mixing in meandering channels with varying bottom topography. J. Hydraul. Res. 15, 351–370. https://doi.org/10.1080/00221687709499640.
Rodi, W., 2017. Turbulence models and their application in hydraulics: a state-of-the-art review. From Mol. Genet. Genomics. https://doi.org/10.1201/9780203734896.
Rozovskii, I.L., 1957. Flow of Water in Bends of Open channels. Academy of Sciences of the Ukrainian SSR: Israel Program For Scientific Translations. available from the Office of Technical Services, U.S. Dept. of Commerce, Kiev (Washington, D.C.
Seminara, G., 2006. Meanders. J. Fluid Mech. 554, 271–297. https://doi.org/10.1017/S0022112006008925.
Seo, I.W., Baek, K.O., 2004. Estimation of the longitudinal dispersion coefficient using the velocity profile in natural streams. J. Hydraul. Eng. 130, 227–236. https://doi.org/10.1061/(ASCE)0733-9429(2004)130:3(227).
Shaheed, R., Mohammadian, A., Yan, X., 2021. A review of numerical simulations of secondary flows in river bends. Water 13, 884. https://doi.org/10.3390/w13070884.
Shapiro, R., 1970. Smoothing, filtering, and boundary effects. Rev. Geophys. 8, 359–387. https://doi.org/10.1029/RG008i002p00359.
Shimizu, Y., Yamaguchi, H., Itakura, T., 1990. Three-dimensional computation of flow and bed deformation. J. Hydraul. Eng. 116, 1090–1108. https://doi.org/10.1061/(ASCE)0733-9429(1990)116:9(1090).
Shin, J., Seo, I.W., 2021. Nonlinear shear effects of the secondary current in the 2D flow analysis in meandering channels with sharp curvature. Water 13, 1486. https://doi.org/10.3390/w13111486.
Shin, J., Seo, I.W., Baek, D., 2020. Longitudinal and transverse dispersion coefficients of 2D contaminant transport model for mixing analysis in open channels. J. Hydrol. 583, 124302 https://doi.org/10.1016/j.jhydrol.2019.124302.
Song, C.G., Seo, I.W., Kim, Y.D., 2012. Analysis of secondary current effect in the modeling of shallow flow in open channels. Adv. Water Resour. 41, 29–48. https://doi.org/10.1016/j.advwatres.2012.02.003.
Stansby, P.K., 2003. A mixing-length model for shallow turbulent wakes. J. Fluid Mech. 495, 369–384. https://doi.org/10.1017/S0022112003006384.
Stoesser, T., Ruether, N., Olsen, N.R.B., 2010. Calculation of primary and secondary flow and boundary shear stresses in a meandering channel. Adv. Water Resour. 33, 158–170. https://doi.org/10.1016/j.advwatres.2009.11.001.
Struiksma, N., 1985. Prediction of 2-D bed topography in rivers. J. Hydraul. Eng. 111, 1169–1182. https://doi.org/10.1061/(ASCE)0733-9429(1985)111:8(1169).
Talmon, A.M., Struiksma, N., Van Mierlo, M.C.L.M., 1995. Laboratory measurements of the direction of sediment transport on transverse alluvial-bed slopes. J. Hydraul. Res. 33, 495–517. https://doi.org/10.1080/00221689509498657.
Termini, D., 2014. In: Bank Erosion and Secondary Circulation in a Meandering Laboratory Flume. 3rd International Geography Symposium. GEOMED2013, Antalya, Turkey, 120, pp. 496–505. https://doi.org/10.1016/j.sbspro.2014.02.129.
Thomson, J., 1877. V. On the origin of windings of rivers in alluvial plains, with remarks on the flow of water round bends in pipes. Proc. R. Soc. Lond. 25, 5–8. https://doi.org/10.1098/rspl.1876.0004.
Uchida, T., Fukuoka, S., 2014. Numerical calculation for bed variation in compound-meandering channel using depth integrated model without assumption of shallow water flow. Adv. Water Resour. 72, 45–56. https://doi.org/10.1016/j.advwatres.2014.05.002.
Uijttewaal, W.S.J., 2014. Hydrodynamics of shallow flows: application to rivers. J. Hydraul. Res. 52, 157–172. https://doi.org/10.1080/00221686.2014.905505.
Uittenbogaard, R.E., van Vossen, B., 2004. Subgrid-scale Model For quasi-2D Turbulence in Shallow Water. Taylor & Francis Group, London, pp. 575–582. https://doi.org/10.1201/9780203027325.ch72.
Valiani, A., Caleffi, V., Zanni, A., 2002. Case study: Malpasset dam-break simulation using a two-dimensional finite volume method. J. Hydraul. Eng. 128, 460–472. https://doi.org/10.1061/(ASCE)0733-9429(2002)128:5(460).
van Balen, W., Uijttewaal, W.S.J., Blanckaert, K., 2010. Large-eddy simulation of a curved open-channel flow over topography. Phys. Fluids 22, 075108. https://doi.org/10.1063/1.3459152.
Van Bendegom, L., 1947. Enige beschouwingen over riviermorfologie en rivierverbeteringen (in Dutch). De Ingenieur 59, B1–B12.
Vanzo, D., Peter, S., Vonwiller, L., Bürgler, M., Weberndorfer, M., Siviglia, A., Conde, D., Vetsch, D.F., 2021. BASEMENT v3: a modular freeware for river process modelling over multiple computational backends. Environ. Modell. Softw. 143, 105102. https://doi.org/10.1016/j.envsoft.2021.105102.
Vermeer, K., 1986. The Ripple Factor in Sediment Transport Equation. Tech. Rep. R657/M1314-V, Toegenpast Onderz, Waterstaat Rivers, Delft Hydraul., Delft, Netherlands.

Viero, D.P., 2019. Modelling urban floods using a finite element staggered scheme with an anisotropic dual porosity model. J. Hydrol. 568, 247–259. https://doi.org/10.1016/j.jhydrol.2018.10.055.

Viero, D.P., D'Alpaos, A., Carniello, L., Defina, A., 2013. Mathematical modeling of flooding due to river bank failure. Adv. Water Resour. 59, 82–94. https://doi.org/10.1016/j.advwatres.2013.05.011.

Viero, D.P., Peruzzo, P., Carniello, L., Defina, A., 2014. Integrated mathematical modeling of hydrological and hydrodynamic response to rainfall events in rural lowland catchments. Water Resour. Res. 50, 5941–5957. https://doi.org/10.1002/2013WR014293.

Viero, D.P., Valipour, M., 2017. Modeling anisotropy in free-surface overland and shallow inundation flows. Adv. Water Resour. 104, 1–14. https://doi.org/10.1016/j.advwatres.2017.03.007.

Wang, D., Tassi, P., 2014. Secondary flow corrections into the telemac-mascaret modelling system. In: Bertrand, O., Coulet, C. (Eds.), Proc. of the 21st TELEMAC-MASCARET User Conference 2014. Grenoble, France, pp. 239–247.

Wei, M., Blanckaert, K., Heyman, J., Li, D., Schleiss, A.J., 2016. A parametrical study on secondary flow in sharp open-channel bends: experiments and theoretical modelling. J. Hydroenviron. Res. 13, 1–13. https://doi.org/10.1016/j.jher.2016.04.001.

Wu, W., Jiang, E., China, P.R., Wang, S.S.Y., 2004. Depth-averaged 2-D calculation of flow and sediment transport in the lower Yellow River. Int. J. River Basin Manag. 2, 51–59. https://doi.org/10.1080/15715124.2004.9635221.

Wu, W., Rodi, W., Wenka, T., 2000. 3D Numerical modeling of flow and sediment transport in open channels. J. Hydraul. Eng. 126, 4–15. https://doi.org/10.1061/(ASCE)0733-9429(2000)126:1(4).

Wu, W., Shields Jr, F.D., Bennett, S.J., Wang, S.S.Y., 2005. A depth-averaged two-dimensional model for flow, sediment transport, and bed topography in curved channels with riparian vegetation. Water Resour. Res. 41, W03015. https://doi.org/10.1029/2004WR003730.

Xiao, Y., Liu, J., Qin, C., Xu, F., 2022. Two-dimensional numerical modeling of flow pattern and bed topography in channel bend. Environ. Model. Assess. https://doi.org/10.1007/s10666-022-09818-5.

Ye, J., McCorquodale, J.A., 1998. Simulation of curved open channel flows by 3D hydrodynamic model. J. Hydraul. Eng. 124, 687–698. https://doi.org/10.1061/(ASCE)0733-9429(1998)124:7(687).

Ye, J., McCorquodale, J.A., 1997. Depth-averaged hydrodynamic model in curvilinear collocated grid. J. Hydraul. Eng. 123, 380–388. https://doi.org/10.1061/(ASCE)0733-9429(1997)123:5(380).

Yeh, K., Kennedy, J.F., 1993. Moment model of nonuniform channel-bend flow. I: Fixed beds. J. Hydraul. Eng. 119, 776–795. https://doi.org/10.1061/(ASCE)0733-9429(1993)119:7(776).